

# Messenger Tagging IR Spectroscopy of Gas-Phase Riboflavin Complexes

Paula Petzschmann

Bachelor Thesis

Department of Molecular Physics  
Fritz-Haber Institute of the Max-Planck Society

Submitted to the  
Department of Physics of Freie Universität Berlin  
for the degree of Bachelor of Science

December 15, 2022

Student ID: 5072959

First Examiner: Prof. Dr. Gerhard Meijer

Second Examiner: Prof. Dr. Tobias Kampfrath

Supervisor: Prof. Dr. Gert von Helden

# Contents

<b>1</b>	<b>Introduction</b>	<b>3</b>
<b>2</b>	<b>Fundamentals</b>	<b>3</b>
2.1	Riboflavin . . . . .	3
2.2	Infrared Spectroscopy . . . . .	4
2.3	Messenger Tagging Infrared Action Spectroscopy . . . . .	7
2.4	Ion Mobility Spectrometry . . . . .	7
2.5	Molecular Modeling . . . . .	9
<b>3</b>	<b>Materials and Methodes</b>	<b>10</b>
3.1	The iMob instrument . . . . .	10
3.2	Free Electron Laser . . . . .	11
3.3	Materials . . . . .	12
3.4	Computational Details . . . . .	12
<b>4</b>	<b>Results and Evaluation</b>	<b>14</b>
4.1	Protonated riboflavin . . . . .	14
4.2	Protonation sites of riboflavin . . . . .	16
4.3	Riboflavin lithium complexes . . . . .	17
4.4	Riboflavin sodium complexes . . . . .	20
4.5	Riboflavin potassium complexes . . . . .	23
4.6	Comparison and discussion of all metal ion riboflavin complexes . . . . .	25
<b>5</b>	<b>Conclusion</b>	<b>27</b>
<b>6</b>	<b>Acknowledgement</b>	<b>29</b>
<b>A</b>	<b><i>CREST</i> input parameters</b>	<b>34</b>
<b>B</b>	<b>Experimental and theoretical CCS values</b>	<b>34</b>
<b>C</b>	<b>Theoretical IR spectra</b>	<b>36</b>
<b>D</b>	<b>Theoretical calculated structures</b>	<b>40</b>

# 1 Introduction

Within the scope of this bachelor thesis, the structural and functional properties of riboflavin were investigated. This includes a detailed analysis of the conformational landscape of riboflavin and its protonation behavior using infrared (IR) action spectroscopy in gas-phase and ion mobility-mass spectrometry.

Riboflavin (Vitamin B2) is found in milk, beer, yeast, and leafy vegetables. It is a yellow-orange compound, which undergoes numerous reactions when exposed to solar radiation. Riboflavin is a precursor to the coenzymes FMN, or riboflavin 5'-phosphate, and FAD.[28] Further, it is known to undergo photoreactions with nucleic acids and used to kill tumor cells and intra- and extracellular HIV.[21]

It is particularly interesting to take infrared spectra of different riboflavin complexes with the method of messenger tagging action spectroscopy, because so far only infrared multiphoton dissociation (IRMPD) spectra of riboflavin complexes were reported in the literature. With messenger tagging action spectroscopy the goal was to measure better resolved IR spectra of different riboflavin alkali metal complexes and to analyse their tendencies for different binding sites within the molecule. Furthermore, the existence of different protonation sites were hypothesized[18], but to date, IR spectra of gas-phase separated riboflavin protomers have not been reported. With the experimental setup used in this bachelor thesis is not only possible to take IR spectra of a conformational and rotational ensemble, but to measure the spectrum of a specific structural conformation, selected beforehand via ion mobility.

In this thesis an overlook over the theoretical foundations of IR spectroscopy and ion mobility is given, along of a description of the experimental setup.

IR spectra, of protonated riboflavin, riboflavin lithium, sodium and potassium complexes were recorded. These spectra are discussed and the structures of the molecules and the different vibrational modes were analysed. Furthermore, the ion mobility of the molecules was analysed with the help of their experimental and theoretical calculated collision cross section (CCS) values.

## 2 Fundamentals

### 2.1 Riboflavin

Riboflavin (Vitamin B2) is found in milk, beer, yeast, and leafy vegetables. It is a orange-yellow compound and it is a precursor to the coenzymes FMN or riboflavin 5'-phosphate and FAD. Riboflavin plays a crucial role in our metabolism and has photoreactive properties that can be used in a clinical context under controlled conditions such as reducing the presence of pathogens in blood products and treating progression of corneal disorders for example keratoconus.[28] Further, it is known to undergo photoreactions with nucleic acids and to sensitize the killing of tumor cells and intra- and extra-cellular HIV.[21]



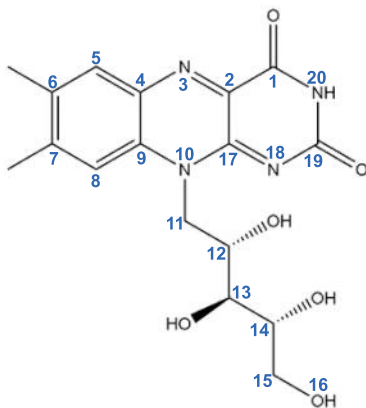


Figure 1: IUPAC enumeration of carbon atoms in riboflavin.

In figure 1 the structural formula of riboflavin is shown and through the numeration, the nomenclature for the different positions of functional groups and distinct atoms that will be used within this bachelor thesis, is set. Riboflavin contains 17 carbon atoms, 20 hydrogen atoms four nitrogen atoms and six oxygen atoms. These atoms form different functional groups in the molecule. As riboflavin is an aromatic, three six-membered aromatic rings build the first functional group, which contains not only ten carbon atoms but also the four nitrogen atoms of the molecule. Two carbonyl groups are located at position (1) and (19), two  $\text{CH}_3$  methyl groups are attached to the aromatic ring system at (6) and (7) and two  $\text{CH}_2$  methyl groups are located at (11) and (15). At position 10 the sugar complex is attached, holding three  $\text{CH-OH}$  secondary alcohol at positions (12), (13) and (14) and one  $\text{CH}_2\text{-OH}$  group of primary alcohol at (15). Looking at previous studies of riboflavin[18] and possible calculated structural conformations, mostly protonation sites at position (19) were observed. Therefore, it was expected to reproduce literature observations in the scope of this thesis.

## 2.2 Infrared Spectroscopy

Irradiating molecules with IR light excites their vibrational states. The energy of the IR photons has to match the difference between the ground and the excited energy level. Most fundamental vibrations appear between 400 and 4000  $\text{cm}^{-1}$ . The wavenumber at which vibrational modes appear, depends on the force constant, functional groups, chemical bonds, and the local chemical environment of the molecule. Thus, it is possible to investigate the structure or conformation of molecules by analysing their IR spectra.[39, 26] Generally, non-linear molecules have  $3N-6$  vibration normal modes, linear molecules have  $3N-5$ . For non-linear molecules, the number of vibrational modes is calculated from the three degrees of freedom for each atom and subtracting the unique molecule translations and rotations. A vibrational mode is IR active, if the vibration of the atoms changes the dipole moment between them. For two atoms of the same mass in a diatomic molecule the potential energy can be described by the Morse potential[25]

$$E(r) = D_e(1 - e^{a(r-r_e)})^2, \quad (1)$$

where  $r$  is the distance between the atoms,  $D_e$  is the dissociation energy,  $r_e$  describes the equilibrium distance and  $a$  is the stiffness constant. The Morse potential takes the anharmonic character into account, by including an exponential increase of the potential for displacements smaller/larger than the equilibrium distance. Since solving the Schrodinger equation using the anharmonic Morse potential is numerically challenging, an approximation of the anharmonic potential by a harmonic potential at small displacements can be beneficial. The bond between two atoms can be treated as a spring, which enables an approximation of the Morse potential by a harmonic potential

$$V(r) = \frac{1}{2}kr^2, \quad (2)$$

where  $k$  describes the spring constant. This approximation does not contain the possibility of dissociation and the anharmonicity of the chemical bond.

For small vibrational energies the Hamiltonian is

$$\tilde{H} = \tilde{T} + \tilde{V} = -\frac{\hbar}{2\mu} \frac{d^2}{dr^2} + \frac{1}{2}kr^2, \quad (3)$$

where  $\mu$  is the reduced mass of two atoms. The stationary Schrödinger equation[37] is

$$\tilde{H}\Psi(r) = E\Psi(r), \quad (4)$$

with the wave eigenfunction  $\Psi(r)$  and the eigenenergy  $E$ . Solving the quantised vibrational energy levels

$$E_n = h\nu \left( n + \frac{1}{2} \right) = \hbar \left( \sqrt{\frac{k}{\mu}} \right) \left( n + \frac{1}{2} \right), \quad (5)$$

where the quantum number is  $n$ , the reduced mass of two atoms is  $\mu$ , and the natural vibrational frequency is

$$\nu = \frac{1}{2\pi} \sqrt{\frac{k}{\mu}}. \quad (6)$$

The photon energy that a molecule can absorb depends on the reduced mass  $\mu$  and the force constant  $k$ .

A common technique to record an IR spectra is measuring the absorption of IR light when passing through the sample. The measured absorption gives insight into the characteristics of the absorbing substance. This is formalized by the Lambert Beer law [40]

$$A(\lambda) = \ln \left( \frac{I_0}{I(\lambda)} \right) = -\sigma(\lambda) \cdot c \cdot d, \quad (7)$$

where  $A$  is the absorbance,  $\lambda$  is the wavelength,  $I_0$  describes the intensity of the light incidence,  $I$  is the intensity of the transmitted light,  $\sigma$  is the absorption cross section,  $d$  is the optical path length, and  $c$  is the concentration.

The technique requires a sufficient sample concentration to keep the path length on a manageable

level. This is only possible for liquid, solid, and gaseous samples with high gas pressure, but when using mass-selecting techniques in the gas-phase, the particle density is not high enough. An extremely long path length would be required for a signal that is distinguishable from background noise. For gas-phase IR spectroscopy a common technique is action spectroscopy. Here the effect of IR absorption is detected and not the absorption itself.[27]

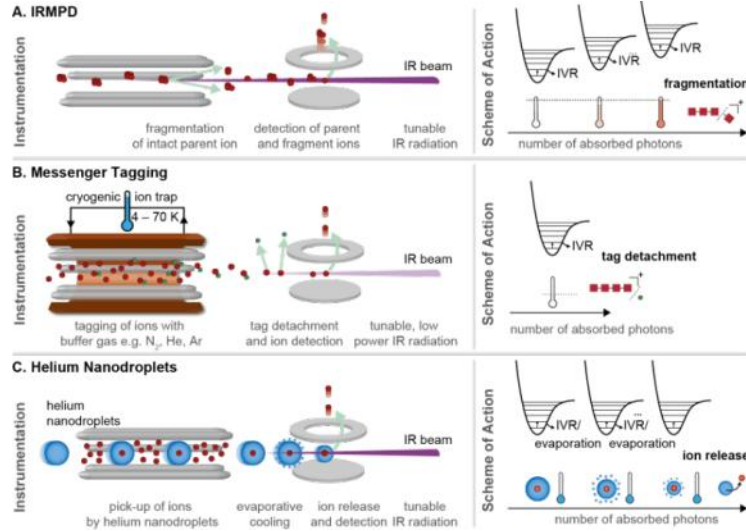


Figure 2: Different types of action spectroscopy, showing the instrumentation and detection scheme of A.) IRMPD, B.) messenger tagging and C.) helium nanodroplets action spectroscopy.

There are different types of IR action spectroscopy. In IRMPD molecular ions are irradiated with an IR light source and absorb photons if the wavenumber of the photon corresponds to the energies of a vibrational mode of the molecule, meaning, if they are in resonance. The sequential absorption of photons will eventually allow the molecule to overcome the dissociation barrier and induces the fragmentation of the ion. An IR spectrum is produced by observing the number of fragment ions as a function of the wavenumber.[14]

In IR spectroscopy with helium nanodroplets the ions get trapped before radiation. Superfluid helium nanodroplets are produced through a precooled reservoir of helium using supersonic expansion. They typically contain around  $10^5$  helium atoms. The droplets pick up the trapped ions and cool them to the equilibrium temperature of 0.37K. Through irradiation with a resonant photon the ion is vibrationally excited and cooled again to its ground state, by heat transfer to the helium matrix resulting in evaporative cooling. This interaction happens several times, till the ion is released from the helium nanodroplet. This is detected as a function of the wavenumber to gain an IR spectrum of the sample of interest. Since the detection of ions does not suffer from extensive background noise, high resolution spectra can be measured.[20]

### 2.3 Messenger Tagging Infrared Action Spectroscopy

In messenger tagging action spectroscopy, a type of action spectroscopy, the ionised molecules of interest enter a cryogenic ion trap where the ions are cooled by collisions to temperatures between 3 to 70 K.[20] Within this thesis, temperatures from 40 to 65 K were applied. The ions are cooled by collisions with a buffer gas, usually helium, argon or nitrogen. In the cryogenic ion trap an interacting messenger atom, in case of this thesis, a nitrogen molecule attaches to the molecule non-covalently. Upon excitation of the messenger tagged ion, the ion is vibrationally excited and undergoes internal vibrational distribution (IVR), allowing the energy to dissipate, eventually resulting in depletion of the messenger tag. The depletion of the tag can be observed as a change in intensity of the mass in a mass analyser. It is visible as an intensity mass shift from tagged ion to parent ion. Contrary to IRMPD it is a one resonant photon process, also the laser energy required for messenger tagging action spectroscopy is significantly lower. Because of this, the line broadening seen in IRMPD can be reduced. A correlation between the tagged and untagged ions can be drawn by the Lambert-Beer law (see equation 7). It defines the number of messenger tagged ions  $N_T(\tilde{\nu})$  for a certain wavelength through

$$N_T(\tilde{\nu}) = N_0 \cdot e^{-\sigma(\tilde{\nu}) \cdot \Phi(\tilde{\nu})}, \quad (8)$$

where  $N_0$  is the number of tagged ions before light interaction and  $\sigma(\tilde{\nu})$  is the absorption cross section, and  $\tilde{\nu}$  is the wavenumber. The photon flux  $\Phi(\tilde{\nu})$  is the number of photons per second and area. This leads to the equation used to plot IR spectra with values of wavenumber against intensity. The observed intensity  $I$  of the transition is defined by

$$I = -\log\left(\frac{N_0}{N_T}\right) \quad (9)$$

### 2.4 Ion Mobility Spectrometry

Ion mobility spectrometry is mostly applied with mass spectrometry (IM-MS) and can be used to analyse the structure of ions and to identify particles in an unknown sample via their ion mobility. There are different experimental operating modes to measure the ion mobility of ions in the gas phase, that to a large extent differ by the properties of the electric field applied. There are different types of IM-MS called traveling wave, trapped, and drift tube IM-M. In travelling-wave ion mobility spectrometry (TWIMS) a periodically changing electric field is applied over the time domain. Radio-frequency voltages of opposite phase are applied to the electrodes and radially confine the ions, while the direct current (DC) moves the ions axially. The DC voltage pulse that is applied to the electrodes creates the travelling wave. Ions of higher mobility are carried by the traveling wave, while ions of lower mobility taking longer to pass the gas-filled mobility cell.[19]

For trapped ion mobility spectrometry (TIMS) ions are accumulated for a fixed time period. During that time the deflection plate is set to a repulsive potential, which directs the ions into the entrance

funnel. They pass through the entrance funnel and the electric field gradient profile until they remain in an equilibrium position. The buffer gas pressure is increased and ions reach their equilibrium position in the tunnel when the drift velocity of the ions through the gas is equal and opposite to the velocity of the buffer gas.[23]

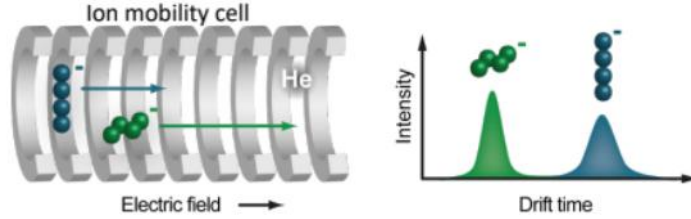


Figure 3: Left: Scheme of a drift tube with two differently shaped ions traveling through the constant electric field. Right: intensity of the detected ions over drift time showing that, for the more expanded ion, it takes a longer time to pass the drift tube.[14]

In drift tube IM-MS the ions enter a drift tube, filled with a buffer gas. In case of this thesis helium was used. A constant, homogeneous, electric field is applied to the drift tube. Ions of different size, charge, and shape travel with different velocities through the drift tube and collide with particles of the stationary gas. Statistically, molecules with a larger rotationally averaged surface area undergo more collisions, thus showing a later arrival time compared to more compact ions. This is schematically illustrated in figure 3. Mass spectrometry filters the ions via their mass-to-charge ratio, while ion mobility is sensitive to their shape.[20] The electric field that is applied to the drift tube is relatively low, because under these conditions the ion velocity is directly proportional to the electric field. The proportionality constant is the ion mobility constant  $K$ . It is defined by the Mason-Schamp equation

$$K = \frac{v_d}{E} = \frac{L}{t_d E} \quad (10)$$

where  $v_d$  describes the drift velocity,  $E$  is the electric field, and  $L$  is the length of the drift tube. The CCS values of ions are physical quantities, which can be compared to calculated CCS values, mostly calculated using the trajectory method.[22, 15, 41]

To calculate the collision cross section (CCS) value from the measured drift time a correction needs to be made, because the measured drift time describes the time span the ions need to not only pass the drift tube, but also the time till they need from the end of the drift tube to the detector. The time the ions need to pass optical instruments after the drift tube to the detector is called  $t_{cor}$ , the actual drift time is called  $t_d$ . Two methods can be used as a correction, the stepped field and the single field method.

For the stepped field method the analyte is injected several times and each time the entrance voltage

$U_1$  is varied. This means each measurement results in a different electric field strength

$$E = \frac{\Delta U}{L} = \frac{U_1 - U_2}{L}, \quad (11)$$

where  $\Delta U$  describes the difference between the entrance and exit voltage and  $L$  is the length of the drift tube. The total drift time is plotted against  $1/\Delta U$ . For the single field method the measurement is made for only one field strength and the experimental CCS value is directly calculated from the measured drift time, by plotting the drift time against CCS values from a CCS standard mix, which contains substances of known CCS values. This results in a straight line plot, described by the equation

$$t_d = \beta y \Omega + t_{cor}, \quad (12)$$

which results out of the Mason-Schamp equation.  $\beta$  is a instrument dependent proportionality coefficient (which depends on gas pressure, electric field, geometry of the drift cell and other ion optics) and  $y$  is the mobility independent flight time.  $\beta$  and  $t_{cor}$  can be calculated by the regression from the slope and intercept

$$y = \frac{1}{z} \sqrt{\frac{m_l}{m_l + m_\beta}} \quad (13)$$

Since the linear equation is directly related to the Mason-Schamp equation, the single field method is substance independent.[12] The collision cross section  $\Omega$  is determined by

$$\Omega = \frac{(18\pi)^{1/2}}{16} \cdot \frac{ze}{(k_b T)^{1/2}} \cdot \left( \frac{1}{m_I} + \frac{1}{m_g} \right)^{1/2} \cdot \frac{t_d \Delta V}{L^2} \cdot \frac{760}{p} \cdot \frac{T}{273.15} \cdot \frac{1}{N_0} \quad (14)$$

where  $e$  is the charge on an electron,  $z$  is the state charge of the analyte ion,  $k_b$  is the Boltzmann constant,  $N_0$  is the number density of the drift gas,  $T$  is the temperature,  $L$  is the length of the drift cell,  $\Delta V$  is the voltage difference,  $p$  is the drift gas pressure,  $t_d$  is the drift time, and  $\mu$  is the reduced mass dependent on  $m_g$  and  $m_I$ , which are the molecular masses of the drift gas and analyte ion.

## 2.5 Molecular Modeling

Techniques for computational analysis of molecules and their interactions is described as "Molecular Modeling". Mechanical and statical methods are more suitable for larger molecules or molecular complexes such as proteins. Quantum chemical methods, on average, yield better results, but are limited to small and medium sized molecules. The wave function of a molecule describes the chemical properties and the interaction between all particles of a system. The wave function can be determined by solving the Schrödinger equation with the molecular Hamiltonian

$$H = T_N + T_e + V_{NN} + V_{ee} + V_{Ne} \quad (15)$$

where  $T_N$  is the kinetic energy of the nuclei,  $T_e$  is the kinetic energy of the electrons,  $V_{NN}$  describes the repulsion between the nuclei,  $V_{ee}$  is the repulsion between the electrons and  $V_{Ne}$  is the attraction

between the electron and the nuclei. An exact solution can only be obtained for very small and simple systems, consisting of a nucleus and an electron. For small to medium sized molecular systems, methods employing different levels of approximations and numerical methods are used.[27] A well known approximation is the Born-Oppenheimer approximation. It uses the difference in mass between nucleus and electron. As the electron is way lighter than the nucleus, the Born-Oppenheimer approximation separates the Schrödinger equation into one equation for the electrons and one equation for the nuclei, to exploit easier solutions of the equations through symmetries. The Hartree-Fock method uses the Born-Oppenheimer approximation.[10, 7] It also uses the mean-field approximation i.e., neglect of the electron correlation. Post-Hartree-Fock methods, such as Møller-Plesset Perturbation Theory or Coupled Cluster[32], include electron correlation[24], which leads to higher precision but are also more costly.

Density Function Theory (DFT) based method use the electron density  $n(r)$  of a system, thus reducing the system from  $n$  variables to three spatial coordinates. DFT based methods are less costly than post-Hartree-Fock methods, but also not as precise.[4] An inhomogeneous, interacting electron gas can be described by the ground state density functional, which was first postulated by Hohenberg and Kohn.[13] Kohn and Sham found a way to calculate the energy by splitting up the kinetic energy into two terms, one calculatable and one correction term, that captures the electron correlation energy and the difference to the exact kinetic energy. Modeling of the correction term is then implemented directly for a variety of density functionals.[33] All DFT functionals can be sorted in a table called Jacob's ladder. This gives an overlook over the quality of the different functionals. The higher the functional appears on the ladder, the better the quality of the results. For hybrid functionals, that appear on the second highest position of the ladder, the exchange energy is partly calculated through DFT and partly through elements of Hartree-Fock theory using the Kohn-Sham orbitals. In this thesis, the hybrid functional wB97XD is used. It includes dispersion and long range corrections, which are important for an accurate description of the aromatic system.[6, 3, 1]

### 3 Materials and Methodes

#### 3.1 The iMob instrument

The gas-phase ions are created by nano electrospray ionization (nESI) using PdPt coated glass capillaries. In the front, the glass capillary forms a tip with a really small diameter. A high voltage is applied, directly to the coated capillary, that creates either positively or negatively charged ions. The ions enters through a heated metal capillary, which is inserted into a stainless steel block. This inlet is at ground potential. The ions exit the capillary into a light vacuum inside the entrance funnel chamber.[38] From there the ions enter the drift tube and pass through the buffer gas, which in case of the iMob is helium or nitrogen. Depending on their mass, charge and structural conformation the ions need a distinct time period to pass the drift tube. This separates the ions based on their ion mobility. A quadrupole mass filter is located right after the drift tube to select a specific  $m/z$  value for the ions that are allowed to pass the quadrupole. The quadrupolar deflector following the

quadrupole mass filter bends the ion beam by  $90^\circ$ . The ion beam is then entering the cryogenic ion trap. The trap is filled with a nitrogen/helium mixture. The ions need to be cooled in order to make the messenger tagging possible.

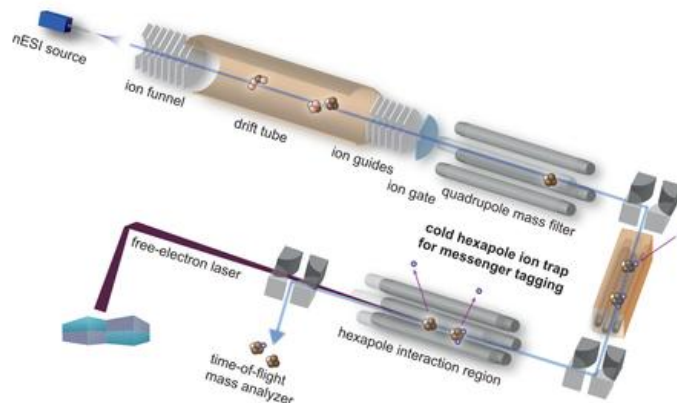


Figure 4: Schematic overview of the iMob instrument

Passing the second quadrupolar deflector the beam of tagged ions is bend again around  $90^\circ$ . Another ion detector is located behind the quadrupolar deflector and can be used to measure the intensity of the ion signal leaving the trap by setting the voltages of the quadrupolar deflector to 0V. If the tagged ion beam is bend it enters the hexapole interaction region. There the ions are overlapped and interact with the laser beam and vibrational excitation and energy redistribution results in tag depletion, which can be measured as an intensity change of for the tagged and untagged species in the Time-of-Flight mass spectrometer (ToF). The ToF is located at the very end of the instrument after the last quadrupolar deflector. After the ions crossed the interaction region, and were bent around by the deflector, they enter the ToF and are subjected to the pusher and puller voltages. Pusher and puller are two extractor plates, which are pulsed with the same frequency as the injection pulse out of the cryogenic ion trap into the interaction region. In positive ion mode the pusher pushes the ions away though a high positive voltage applied, then the puller pulls the ions with a high negative voltage. The ToF is operated in V-Mode which means the ions are only reflected one time.[14, 20]

### 3.2 Free Electron Laser

Action spectroscopy depends on the number of molecules of the analyte in the gas phase and requires a high photon flux. Tabletop lasers are often not able to provide a high enough photon flux. Free electron lasers can provide radiation of high power over a wide spectroscopic range. Firstly, electron packages are produced by the electron gun with a 1 GHz micro-pulse repetition rate. These electron bunches get accelerated by the linear accelerators till they reach a kinetic energy between 15 to 50 MeV. As the electrons packages are bend into the laser cavity, they are passing through a magnetic field that forces the electrons on a sinusoidal path perpendicular to the field. This part of the FEL



is called undulator. The undulator is about 2 m long and contains NdFeB permanent magnets. These magnets force the electrons into a sinusoidal orbits radiate electromagnetic waves of a certain frequency.[14]

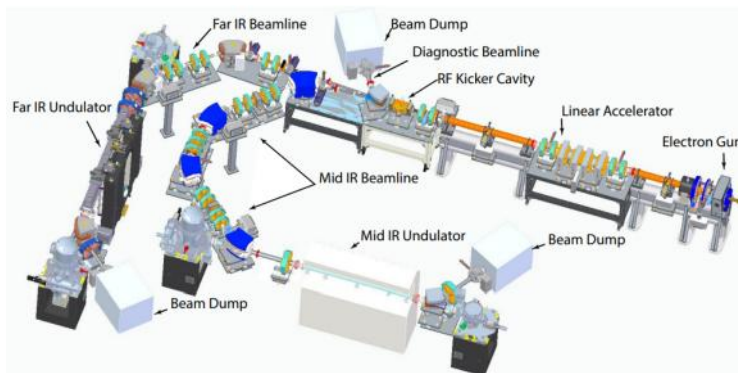


Figure 5: Schematic overview of the Fritz Haber Institute free electron laser, figure adapted from literature.[34]

Through this wiggling motion the radiation is emitted. Its wavelength is determined by the electron energy and the gap between the NdFeB permanent magnets on top and on the bottom of the undulator. The radiation is reflected multiple times with a gold plated laser cavity mirror and overlapped with more electron beams that produce more radiation by being forced on their sinusoidal path. The IR beam is then let out through a hole in the mirror.[20] The FEL at the Fritz-Haber-Institute provides IR radiation from 4 to 50  $\mu\text{m}$  using a mid-IR beamline. The electrons are ejected by the electron gun, then they enter a region with two linear accelerators which set the electrons energy. The electron energy is around 15 to 50 MeV.[35, 36, 9]

### 3.3 Materials

A stock solution of riboflavin in water with a concentration of 150  $\mu\text{M}$  was prepared. For protonated riboflavin the stock solution was diluted in Water/Methanol (v/v, 20/80 %) to a concentration of 50  $\mu\text{M}$  to which 1 v/v % formic acid was added. Riboflavin sodium complex was prepared in the same way, except no formic acid was added. For the preparation of riboflavin lithium, and potassium complexes, riboflavin was diluted to a concentration of 150  $\mu\text{M}$  and 1eq of LiCl and KCl was added, respectively. For the experiments, the stock solution was diluted in water/methanol (v/v, 20/80%) to a concentration of 50  $\mu\text{M}$ . During the optimisation of the spraying conditions, it was found that the optimal ionization efficiency was reached in excess of LiCl and KCl (40eq and 60eq of LiCl and KCl were added, respectively).

### 3.4 Computational Details

Screening of protonation and alkalation sites, as well as exploration of the conformational space, were performed using the *CREST* software suite.[29] In a first step, possible candidate structures for

a conformational search were generated using the *CREST* protonation and alkalation submodule. A summary of the command line invocations can be found in the appendix (see Table 1). The generated protonated and alkalated structures were subjected to the meta-dynamics and static meta-dynamics conformer-rotamer sampler iMTD-sMTD to identify the lowest energy conformation (see Table 2).[30] For each input structure, the lowest energy conformer was identified and its geometry used in a subsequent geometry optimization and harmonic frequency calculation at the wB97XD/def2-TZVP [2] level of theory using the Gaussian<sup>®</sup> g16 program.[8] For the comparison between theory and experiment, experimental IR spectra were extracted from the measured time-of-flight mass spectra over the time and laser wavelength domain of the experiment. In a first order approximation, the accumulated intensity values were normalized to the energy and repetition rate of the laser. The theoretically calculated harmonic frequency line spectra were convoluted using a Gaussian kernel with a dynamic convolution width. Here, the width of the convolution at the respective harmonic frequency is determined from the width of the laser at the same frequency. In cases where the convolution had to be extended beyond the measurement range, the last experimentally determined width was used for all following convolutions. The theoretical IR spectra were finally scaled (harmonic energy correction) by multiplication with vibrational scaling factor of 0.955 (wB97XD/def2-TZVP).[31] Calculations of theoretical CCS values were performed using a customized version of the Mobcal-MPI software.[16] The required Merz-Kollman charges were calculated at the wB97XD/def2-TZVP level of theory by specifying the pop=(MK,ReadRadii) keyword. For K, a Van-der-Waals radius of 2.75 Å was specified as it is not a predefined value in the g16 program.[11] Experimental CCS values were calculated using an in-house developed script for calculation of drift tube CCS values from voltage dependent arrival time measurements.

## 4 Results and Evaluation

IR spectra of protonated riboflavin and riboflavin lithium, sodium and potassium complexes were measured. For all measurements the theoretical spectra and corresponding energies were calculated. Furthermore the CCS values were measured and theoretically calculated.

### 4.1 Protonated riboflavin

The IR spectra of protonated riboflavin were taken to gain a better understanding of riboflavins protonation preference and the associated structural conformation. It was measured from 1000-1900  $\text{cm}^{-1}$ . The IR spectrum of protonated riboflavin is depicted in figure 6. In the following discussion, prominent IR bands important to the structural understanding of protonated riboflavin are given in alphabetical order from high to low wavenumbers. It shows two strong vibrational modes at 1795 and 1780  $\text{cm}^{-1}$ , labeled (L) and (K). Peak (J) has high intensity and is located at 1610  $\text{cm}^{-1}$ , peak (I) appears at 1575  $\text{cm}^{-1}$ . Bands (H) and (G) from 1575-1400  $\text{cm}^{-1}$  have lower intensity. Band (F) is located at 1335  $\text{cm}^{-1}$  and peak (E) appears close to (D) at 1265  $\text{cm}^{-1}$ . Band (D) at 1230  $\text{cm}^{-1}$ , and band (C) at 1170  $\text{cm}^{-1}$ , show similar vibrational intensity. Lastly (B) and (A) at 1105 and 1045  $\text{cm}^{-1}$  have lower intensities.

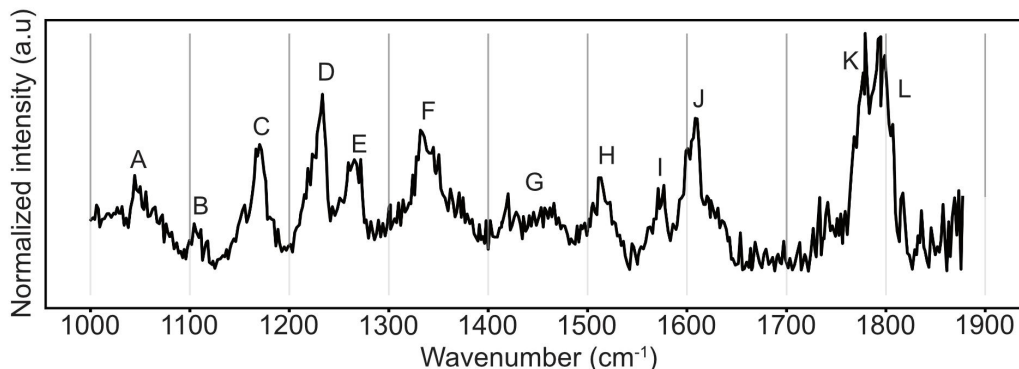


Figure 6: IR spectrum of protonated riboflavin in the range of 1000-1900  $\text{cm}^{-1}$ .

The double peak (L) and (K) have main contribution from the C=O stretching motion of the molecule, as C=O stretching vibrations appear usually around 1800  $\text{cm}^{-1}$ .<sup>[17]</sup> The aromatic C=N and C=C stretching modes of the ring system are assigned to (H),(I) and (J), with (J) showing overall highest intensity. Peak (E), (F) and (G) have contribution of the different vibrational modes of  $\text{CH}_3$ - and  $\text{CH}_2$  groups of the molecule. Peaks (D) to (A) do most likely hold C-OH deformation modes or CH bending motions of the aromatic ring system, which appear between 1250 and 950  $\text{cm}^{-1}$ .<sup>[5]</sup>

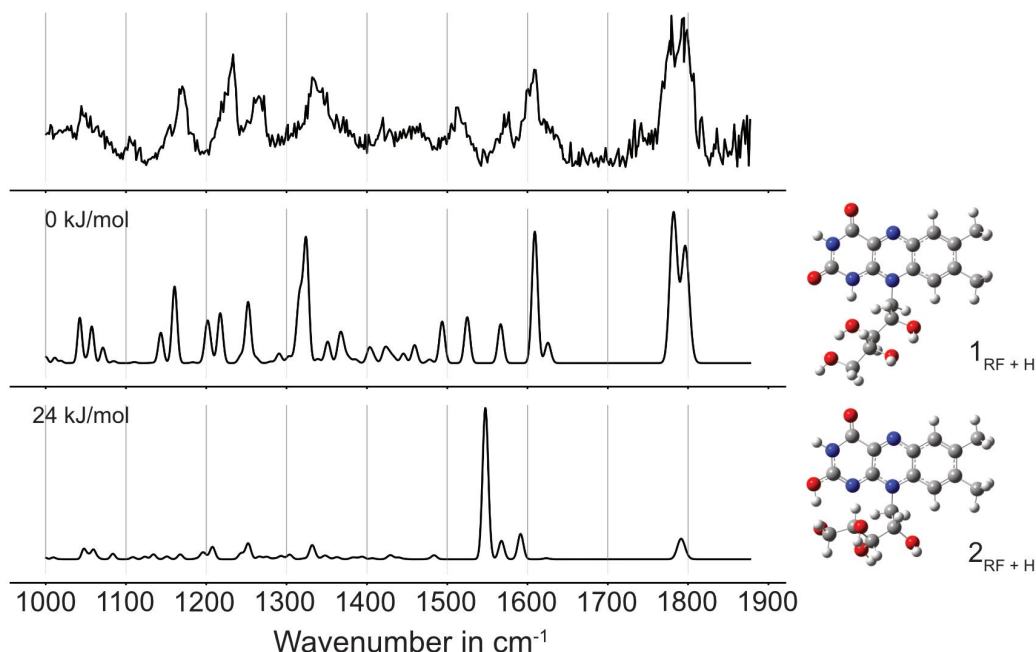


Figure 7: Experiment and theory comparison of protonated riboflavin calculated at the wB97xD/def2-T2VP level of theory. Shown here are the two lowest energy structures ( $\leq 30$  kJ/mol).

For a structural assignment of the observed vibrational transitions, the theoretical structures and associated spectra were calculated (see chapter 3.4). Figure 7 shows the two lowest energy structures in comparison to experimental IR spectrum. Peak to peak comparison of their positions and intensities, reveals that the lowest energy structure shows the best agreement with the experiment. As shown in figure 7, the first theoretical spectra depicts the structure of riboflavin, with the hydrogen atom attached at position (18). Upon inspection, the different peaks and their belonging vibrational modes shows the accuracy of the predicted ones. The theoretical analysis showed some vibrational modes, that could not be confidently assigned previously. As the spectra is such a good fit, it is most certainly the structure  $1_{RF+H}$  that was measured. Therefore, it is relevant to further inspect the vibrational modes of the experimental spectrum in comparison to the lowest energy theoretical spectrum. Starting with (K) and (L), both peaks do not only hold the C=O stretching vibration, but also a NH bending motion at position (20) and in both cases with contributions from the other C=O-stretching vibration with a smaller displacement vector. It also holds a bending motion of the NH at position (18), the protonation site. For peak (J) the same NH-Bending motion at position (18) was observed. (J) to (H) hold C=C, and C=N stretching motions. (I) was also assigned to a CH bending motion of the aromatic ring system and (H) gets assigned to a CH-Bending motion of the aromatic ring system, a CH<sub>2</sub> scissoring and symmetric CH<sub>3</sub> vibration. As (H) is not clearly assigned to one peak of the theoretical spectrum, it might not necessarily hold CH<sub>2</sub> or CH<sub>3</sub> vibrational modes as they can be assigned to the lower one of the two peaks at 1494 cm<sup>-1</sup>. (H) is a little closer to the peak higher in wavenumber at 1525 cm<sup>-1</sup>. Vibrational modes of the methyl group usually appear between 1550 to 1300 cm<sup>-1</sup>. [17] Region (G) could not be allocated very clearly

in the theoretical spectra, but the theoretical spectra, showed that there are CH<sub>2</sub> scissoring and symmetric CH<sub>3</sub> deformation vibrations. (E) showed a CH<sub>2</sub> twisting and also a CH bending motion of the sugar complex. Both (C) and (D) hold a CH bending motion of the aromatic ring system and different CH<sub>2</sub> and CH<sub>3</sub> vibrational modes, which usually do not appear in wavenumber regions this low. It is not certain that the calculation is accurate in this case, as there could be no reason found for these methyl vibrations to appear this low. (B) can not be assigned to any peak in the theoretical spectra. (A) showed C-OH bending, and stretching motions.

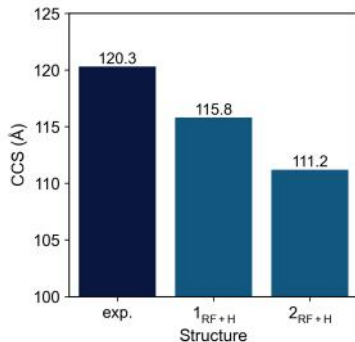


Figure 8: CCS values of protonated riboflavin structures calculated with MOBCAL-MPI in comparison to the experimentally determined CCS value.

Evaluating the CCS measurement and theoretical CCS calculations, figure 8 clearly indicates that structure 1<sub>RF+H</sub> best fit the experimental measurement in regard to CCS-values. The observed discrepancy between the experimental and best fitting theory CCS value is within the range of reported errors of the MOBCAL-MPI software ( 4%). Thus, the root cause may originate from deviations in the experimental pressure value, but also in the ion-buffer gas interaction model. Combining the results of IMS and cryogenic IR spectroscopy, the conclusion can be drawn that structure 1<sub>RF+H</sub> (for nomenclature and structures see appendix) is actually the one that was measured. The other spectra do not match nearly as well.

## 4.2 Protonation sites of riboflavin

In literature[18], the presence of more than one protonation sites was discussed, however, to-date experimental approaches using cold ion spectroscopy were missing an ion mobility dimension. As described before, the instrument enables not only to take the measurement of IR spectra of a certain molecule, but also the selection the ions via their ion mobility. This ensures that the IR spectra taken is of one specific conformation or in this case of one specific protomer.

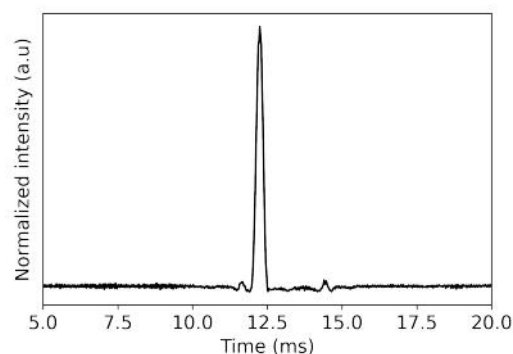


Figure 9: Arrival time distribution of protonated riboflavin measured on the iMob Instrument using a nano-electrospray source.

Protonated riboflavin was sprayed on the iMob instrument. The arrival time distribution after mass selection was measured, and, as indicated in figure 9, different peaks were observed: one peak of significantly high intensity and lower intensity peaks. More than one peak in the arrival time after mass selection demonstrate the existence of a multitude of conformations. After tuning for all peaks in the arrival time distribution and subsequent high resolution mass to charge determination in the TOF, it was revealed that all minor peaks do not fit the riboflavin mass and are impurities. This indicates there are no protomers of riboflavin visible on the iMob instrument. To verify this observation the sample was also assessed on a Bruker TIMS-TOF instrument for better resolution. Only one peak is visible in the mobilogram taken on the TIMS-TOF shown in figure 10, meaning only one protonation site of riboflavin was detected.

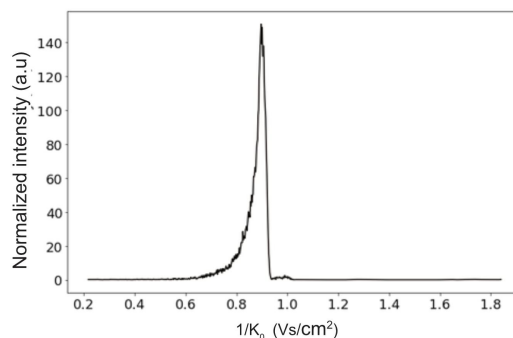


Figure 10: Mobilogram of protonated riboflavin measured on the Bruker TIMS-TOF Instrument.

### 4.3 Riboflavin lithium complexes

As previously outlined, the different metal ion riboflavin complexes will now be analysed. Differences in peak positions and intensities of the IR spectra were expected depending on the different alkali atoms and the complexation motif in riboflavin. In both this and the following two chapters, the IR spectra of metal ion riboflavin complexes will be discussed and later on compared to theory.

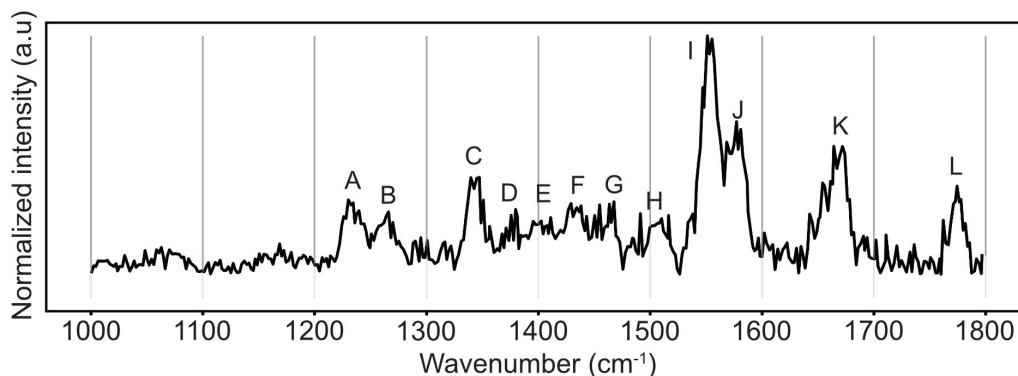


Figure 11: IR spectra of the riboflavin lithium complex in the range of 1000-1800  $\text{cm}^{-1}$ .

The spectrum visualised in figure 11 shows peak (L) and (K) at 1775 and 1670  $\text{cm}^{-1}$ . Peak (J) and (I) of high intensity are located at 1575 and 1555  $\text{cm}^{-1}$ . Peaks (H) at 1510  $\text{cm}^{-1}$  has smaller intensity. From 1480 to 1350  $\text{cm}^{-1}$  peaks (G) to (D) appear and peaks (C), (B) and (A) between 1200 to 1350  $\text{cm}^{-1}$ , have smaller intensities. Peak (L) and (K) hold the C=O stretching vibrations of the molecule. Peak (I) has strong contribution from C=N and C=C stretching modes of the aromatic ring system as well as peak (J). Band (B) and (A) are most likely CH bending motions of the aromatic ring system. (G) to (C) most likely hold all kinds of methyl vibrational modes. (H) is not clearly assignable to one vibrational mode, as it appears in a wavenumber region that lies between the areas where C=C, C=N stretching vibrations and methyl vibrational modes usually appear. Looking at the calculated spectra for lithiated riboflavin in figure 12, four very similar looking spectra (just the spectrum of structure  $4_{RF+Li}$  looks different in the region of 1600-1800  $\text{cm}^{-1}$ ) are depicted. It becomes evident that there are bands in the region from 1000-1200  $\text{cm}^{-1}$  not resolved in the experimental spectrum that was taken. The rest of the spectra fits the experimental spectrum accurately, especially the structure  $1_{RF+Li}$  that is also the best match energywise. Looking at all four structures that were calculated, the alkali atom is always weakly bonded to the carbonyl group, bond at position (19) of the molecule. It is likewise attached to the two oxygen atoms of the sugar complex of the molecule. In case of  $3_{RF+Li}$  the atom formed a bond with the nitrogen at position (18) but is still close to the C=O-Bond.

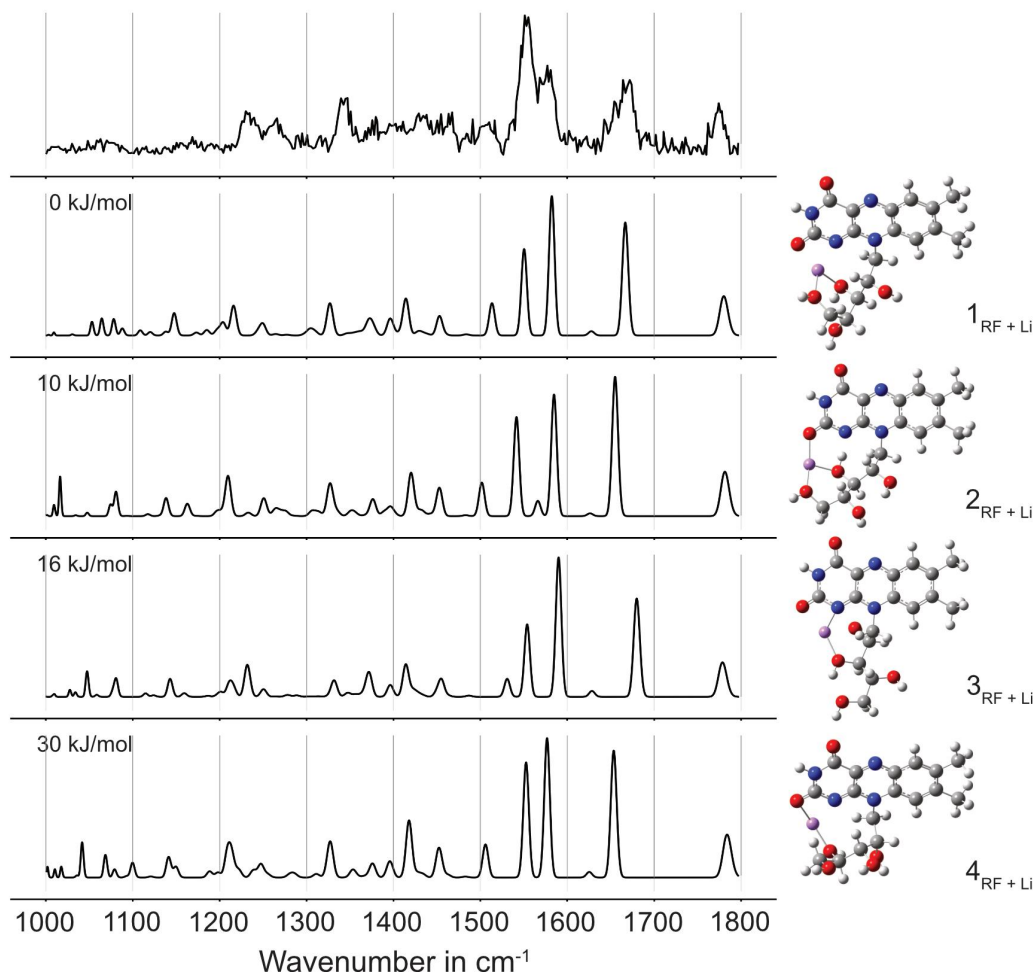


Figure 12: Experiment and theory comparison of riboflavin lithium complexes calculated at the wB97xD/def2-T2VP level of theory. Shown here are the two lowest energy structures ( $\leq 30$  kJ/mol).

Analysing the spectra of the best structural match assists in the assignment of (H) to contributions from C=C, C=N stretching vibrations and a CH<sub>2</sub> scissoring motion. This is in good agreement with literature values reported for this wavenumber region.[17] (C) to (G) hold symmetric and antisymmetric CH<sub>3</sub> and different CH<sub>2</sub> vibrational modes, more precisely wagging, twisting and scissoring. (B) does not only hold a CH bending motion of the aromatic ring system, but likewise a CH<sub>2</sub> twisting motion according to the calculation. This is not very likely, knowing that Methyl vibrational motions usually appear between 1550 to 1300 cm<sup>-1</sup>. [17] Peak (A) holds not only a CH bending motion of the aromatic ring system but also a C-OH bending motion and a NH bending motion at position (20). Structures differ by the orientation of the ribotyl unit, leading to overall very similar spectra.



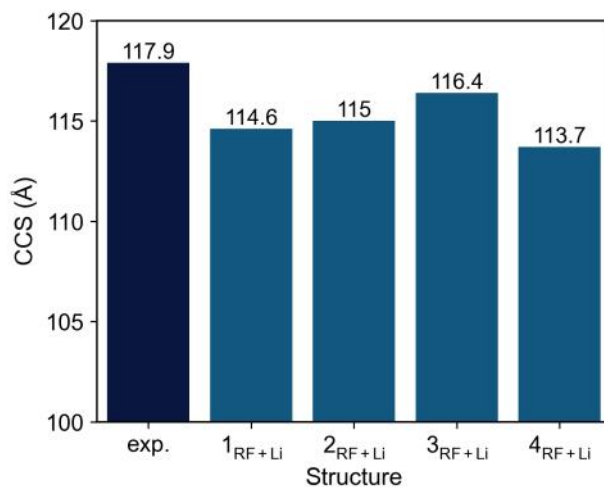


Figure 13: CCS values of structures of riboflavin lithium complexes calculated with MOBCAL-MPI in comparison to the experimental determined CCS values.

The calculated CCS values shown in figure 13 are all rather similar. Although they differ from the experimental value, as described before all calculated CCS values are significantly lower than the experimental value.

#### 4.4 Riboflavin sodium complexes

The second metal ion riboflavin complex investigated was the riboflavin sodium complexes. It is slightly heavier than lithium with a mass of 22,99 u. The spectrum was measured from 1000-1800  $\text{cm}^{-1}$ . The assignment of the peaks is identical to the previously reported labels for riboflavin sodium complexes.

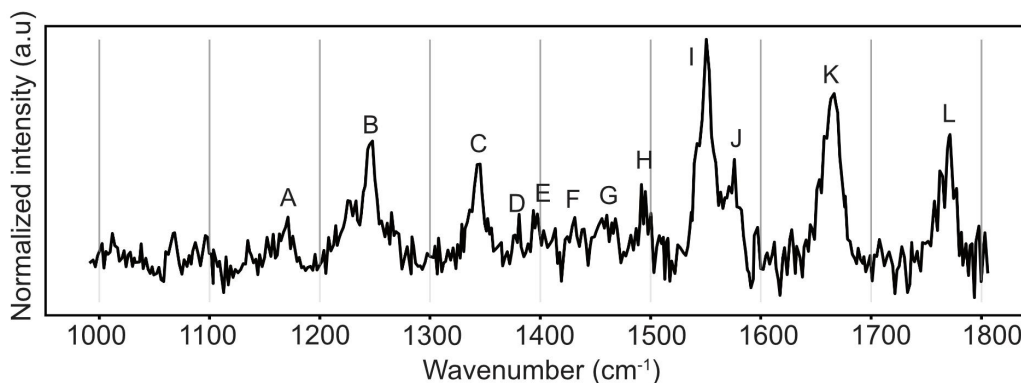


Figure 14: IR spectrum of the riboflavin sodium complex in the range of 1000-1800  $\text{cm}^{-1}$ .

Figure 14 shows the very prominent C=O stretching vibrations appearing as peaks (L) and (K), followed by peaks (J) and (I) holding the C=N, and C=C stretching vibrations of the aromatic ring system. C=C and C=N stretching vibrations are located between 1625 and 1575  $\text{cm}^{-1}$ . [5]

Peaks (G) and (C) hold different vibrational modes of the  $\text{CH}_3$  and  $\text{CH}_2$  groups of the molecule. (H) cannot be clearly assigned to one vibrational mode, as it appears between the region for methyl vibrational modes and the region for  $\text{C}=\text{C}$  and  $\text{C}=\text{N}$  stretching vibrations. Peaks (A) and (B) might have contributions from CH bending motions of the aromatic ring system or C-OH bending motion of the sugar unit. CH bending motions do appear around  $1250$  to  $950\text{ cm}^{-1}$  [5] and C-OH motions appear around  $1300$  to  $1400\text{ cm}^{-1}$ . [17]

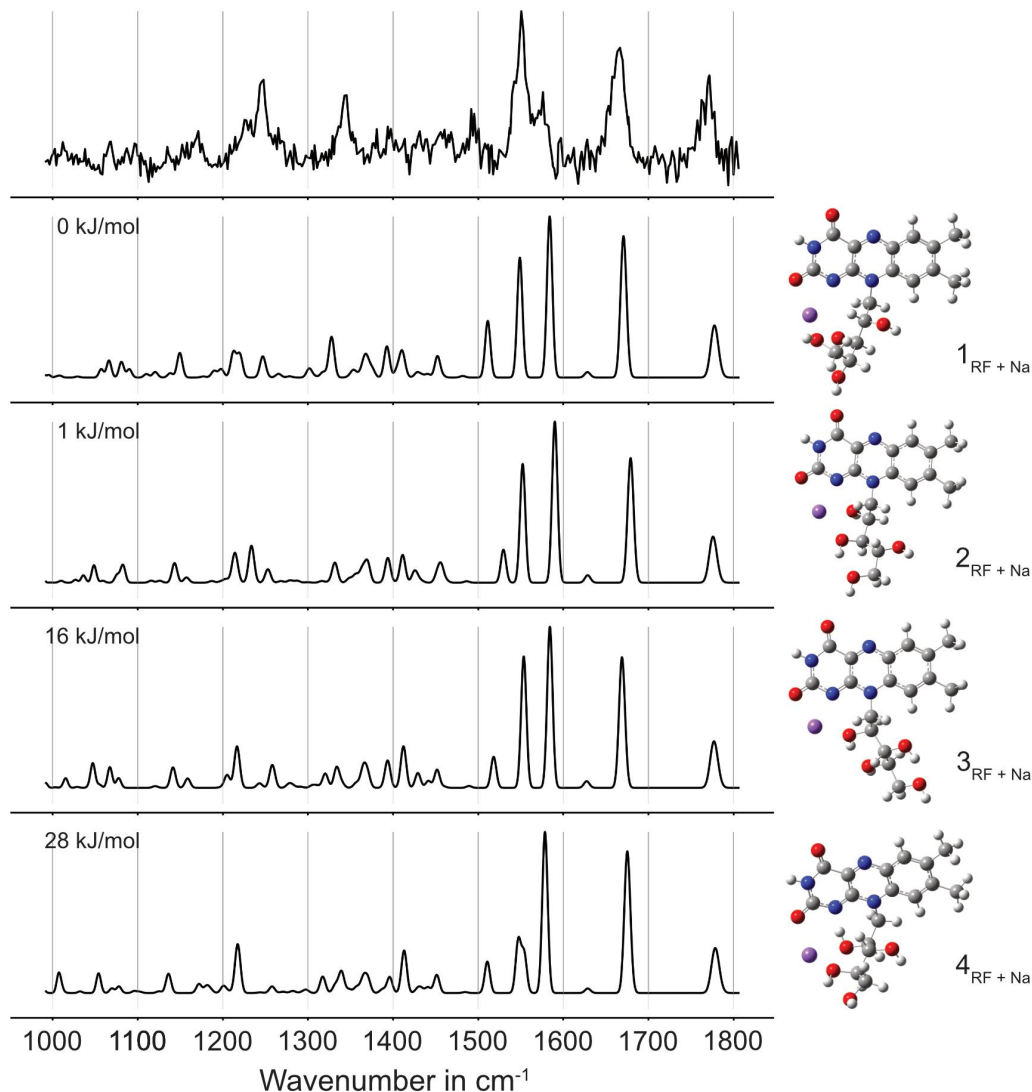


Figure 15: Experiment and theory comparison of riboflavin sodium complex calculated at the wB97xD/def2-T2VP level of theory. Shown here are the two lowest energy structures ( $\leq 30\text{ kJ/mol}$ ).

A look at all theoretically calculated spectra of riboflavin sodium complexes shown in figure 15 revealed not many differences but rather many similarities. The sodium atom is attached near the carbonyl group position (19). Merely the sugar complex of the molecule is oriented differently among the theoretical structures. The peak position and intensity matches the experimental

spectra accurately. Upon closer inspection of the best matching spectra, it was possible to assign the vibrational modes with higher accuracy. Although peak (H) and (J) do not precisely fit the theoretical spectra, it can be confirmed that the assignment of peaks (H) to (L) was again identical. (K) and (L) do not only hold the C=O stretching vibrations, but a bending motion of the NH at position (20). From (D) to (G) different CH<sub>3</sub> (and CH<sub>2</sub>) vibrational modes were assigned. Theory reported those as CH<sub>2</sub>-wagging, mostly antisymmetric CH<sub>3</sub> deformation vibrations, but also symmetric CH<sub>3</sub> deformation vibrations. (D) also holds a NH, and a C-OH bending motion. (B) does not only hold a CH bending motion of the aromatic ring system, but may hold a CH<sub>2</sub> twisting motion, a CH<sub>2</sub> wagging motion, C-OH bending motion and a CH bending motion located at the sugar unit. In the region from 1000 to 1200 cm<sup>-1</sup> all theoretical spectra showed bands of low intensity, which are not all resolved experimentally. It is most certainly a CH bending motion, as they commonly appear in this region and the theoretical spectra shows weak to strong CH bending motion between 1160 and 1210 cm<sup>-1</sup>. (A) is located at 1170 cm<sup>-1</sup>. In the region from 1000 to 1200 cm<sup>-1</sup> the calculated spectra also shows a CH<sub>2</sub>-twisting motion around 1141cm<sup>-1</sup>, which is not very likely to actually take place there, knowing that they usually appear at higher wavenumber regions.[17] Despite the fact that the theoretical best matching spectrum fits the experimental spectrum really well it does not differ very much from the other calculated structures. This means it is unclear if the 1<sub>RF+Na</sub> is the structural conformation that was measured. Probably, the sugar unit is very flexible and an ensemble of different conformations was measured. This is also supported by the rather similar CCS values, shown in figure16. However, information about the structure was still gained. In every calculated structure, the added atom attaches near the C=O bond at position (19), which leads to the conclusion that a structural conformation with this attribute must have been measured and is energetically favored due to the chelating effect of the sugar hydroxyl groups and the carbonyl group.

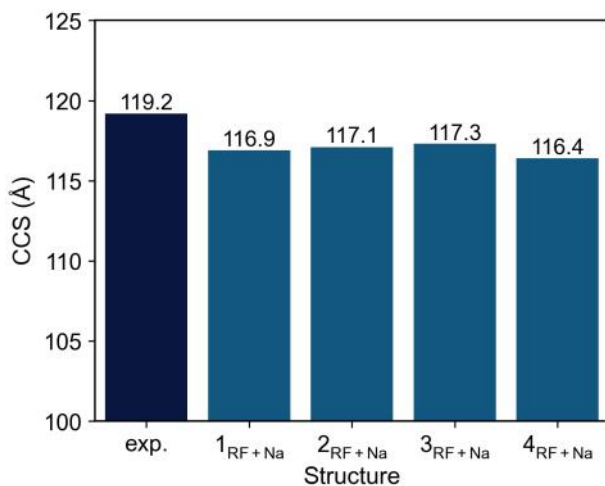


Figure 16: CCS values of structures of riboflavin sodium complexes calculated with MOBCAL-MPI in comparison to the experimental determined CCS values.

## 4.5 Riboflavin potassium complexes

The spectrum of riboflavin potassium complexes shown in figure 17 has two strong peaks (I) and (L), which are located at 1550 and 1675  $\text{cm}^{-1}$ . The next significant peak (K) is located at 1775  $\text{cm}^{-1}$ . Peak number (I) is a double peak with second component (J) at 1485  $\text{cm}^{-1}$ . Five bands with lower intensity than the other ones were observed between 1350 and 1500  $\text{cm}^{-1}$  and labeled from (H) to (D). Two bands of lower intensity are (C) and (B) at 1250 and 1230  $\text{cm}^{-1}$ . The lowest energy band assigned is (A) at 1100  $\text{cm}^{-1}$ .

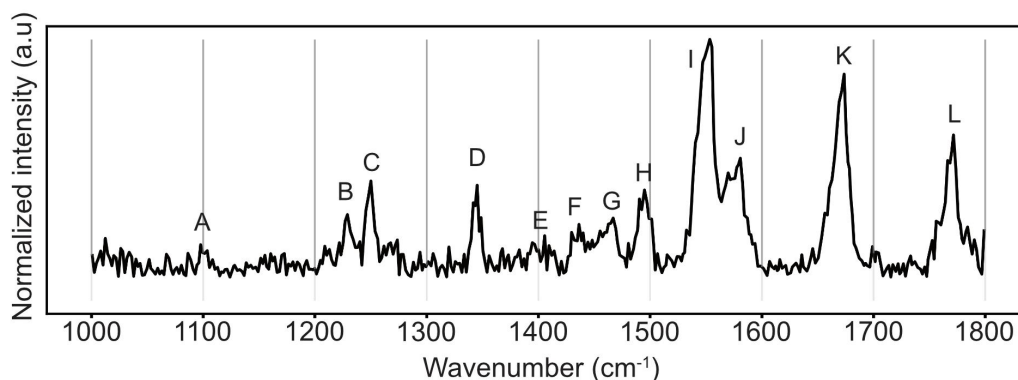


Figure 17: IR spectrum of the riboflavin potassium complex in the range of 1000-1800  $\text{cm}^{-1}$ .

One C=O stretching vibration is observed at 1770  $\text{cm}^{-1}$ . The other C=O stretching of the molecule is located at 1675  $\text{cm}^{-1}$ . The band (J) and (I) are both C=C, and C=N stretching vibrations of the aromatic ring system of the molecule. The peaks (G) to (D) are of lower intensity and are most likely to be vibrational modes of the  $\text{CH}_2$  and  $\text{CH}_3$  groups of the molecule. Peak (A) to (C) have contribution from the in-plane bending motion of aromatic ring, which might be complemented by C-OH bending motions that usually appear between 1260-1440  $\text{cm}^{-1}$ . [17] The IR spectrum for the lowest energy structure calculated is in good agreement with the experimentally measured spectrum. Peaks in the experimental spectrum match peak position and intensity of the lowest energy structure, with slight deviations in position for (H) to (E) and in intensity for (J) and (I). However, due to the nature of the harmonic calculation, anharmonicities are not accounted for, which might explain these smaller deviations. Taking a closer look at the theoretical spectra shown in figure 18 it becomes evident that, in comparison, all of them show clear similarities. Furthermore, the calculated structural conformations do not differ a lot. As with Riboflavin with lithium, the added potassium forms at least one bond with one of the oxygen atoms of the sugar unit. It is always located closer to the C=O bond at position (19), as it is the case for all other alkali atoms. Although structure  $3_{RF+K}$  indicates stabilizing contributions from the nitrogen at position (18), it may not be as favored to from due to the decreased stabilizing effect of the linearly extended sugar unit, thus favoring  $1_{RF+K}$  overall. Knowing that the spectra and belonging structures are very similar, it is again hard to clearly decide which one was measured. But the best match that was found is in good agreement.

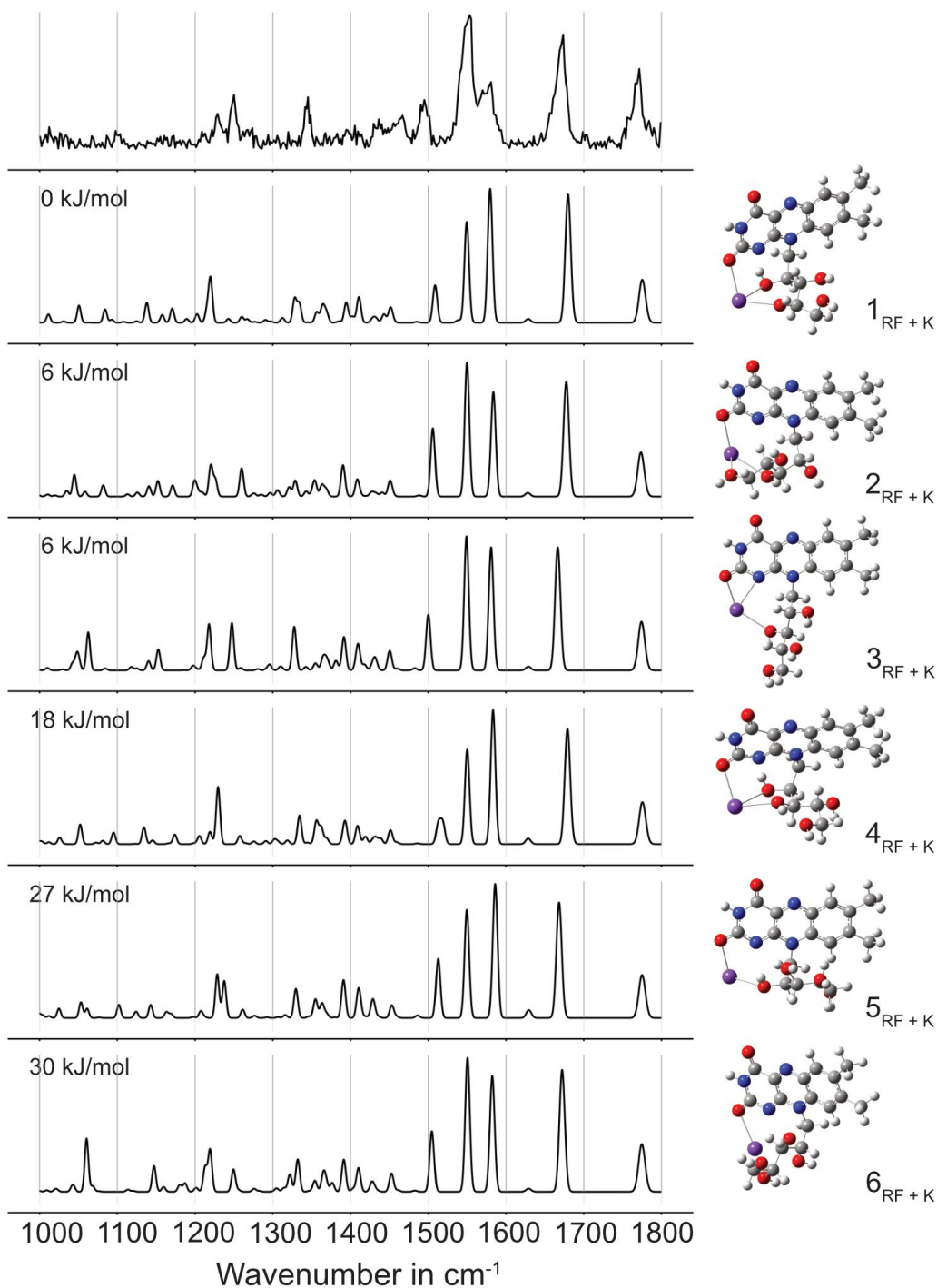


Figure 18: Experiment and theory comparison of riboflavin potassium complexes calculated at the wB97xD/def2-T2VP level of theory. Shown here are the two lowest energy structures ( $\leq 30$  kJ/mol).

Analysing the spectra of  $1_{RF+K}$  in detail, leads to specific assignment of some vibrational modes. Theory supports the assignment of (L) to (H) that was previously made, but shows a second component for (K) and (L), the NH bending motion. A look at the position of the C=O bonds

in the molecule shows that it is close to the NH bond in motion. Therefore, the C=O stretching vibrations are in close chemical environment to the NH bending motion and therefore it would be surprising to see a decoupled movement of the nitrogen and hydrogen. An interesting observation is that peak (K) comprises contribution of the hydroxyl group C-OH bending motion, that is involved in the stabilization of the potassium. (J) is likely to have contribution from CH bending motion of the aromatic ring system, which probably results out of the strong C=C stretching motion. Peaks (G) to (D) seem to actually hold different CH<sub>2</sub> and CH<sub>3</sub> vibrational modes, although these peaks are not clearly allocatable in the theoretical spectra. It is still possible to get a better idea which vibrational modes contribute despite the fact that the experimental spectrum does not look identical in this region. In this region CH<sub>2</sub> scissoring, wagging and twisting motions, and symmetric and antisymmetric CH<sub>3</sub> deformation vibrations can be found. A CH<sub>2</sub> twisting motion is theoretically assigned to (A), (B) and (C). Again (B) and (C) are not differentiable. For the wavenumber region they are in, it is very unlikely to hold a CH<sub>2</sub> vibrational mode, as they appear in higher wavenumber regions. (A) does hold a C-OH stretching motion and (B)/(C) holds C-OH bending motions (and CH bending motions of the aromatic ring system) and a NH-Bending motion at position (20). Looking at region 1000-1200 cm<sup>-1</sup> it gets clear that only one of the peaks that seem to be located in this area was actually resolved in the measured spectrum. Looking at the vibrational modes of the theoretical spectra a CH bending motion of the aromatic ring system, as in literature predicted, appears.[5] The CCS values are shown in figure 19. The theoretical values differ within each other, because of the low energy barrier it is possible, that just 1<sub>RF+K</sub> and 2<sub>RF+K</sub> or just 3<sub>RF+K</sub> is visible and measured experimentally. As mentioned previously, the calculated CCS values have a systematic error, therefore the calculated values are systematically smaller than the experimental value.

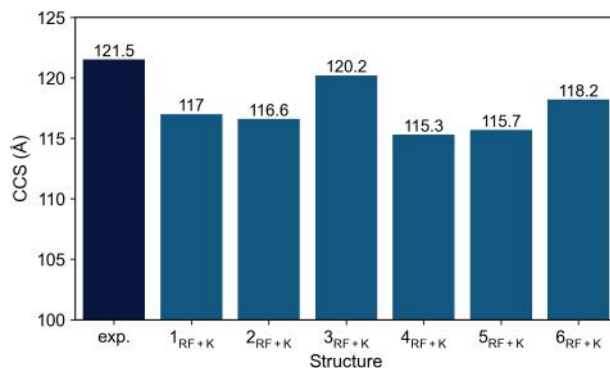


Figure 19: CCS values of structures of riboflavin potassium complexes calculated with MOBCAL-MPI in comparison to the experimental determined CCS values.

#### 4.6 Comparison and discussion of all metal ion riboflavin complexes

Graphic 20 shows all three IR spectra of metal ion riboflavin complexes in comparison. Previously assumed was that there would be changes visible in the spectra depending on the alkali ion measured with riboflavin.



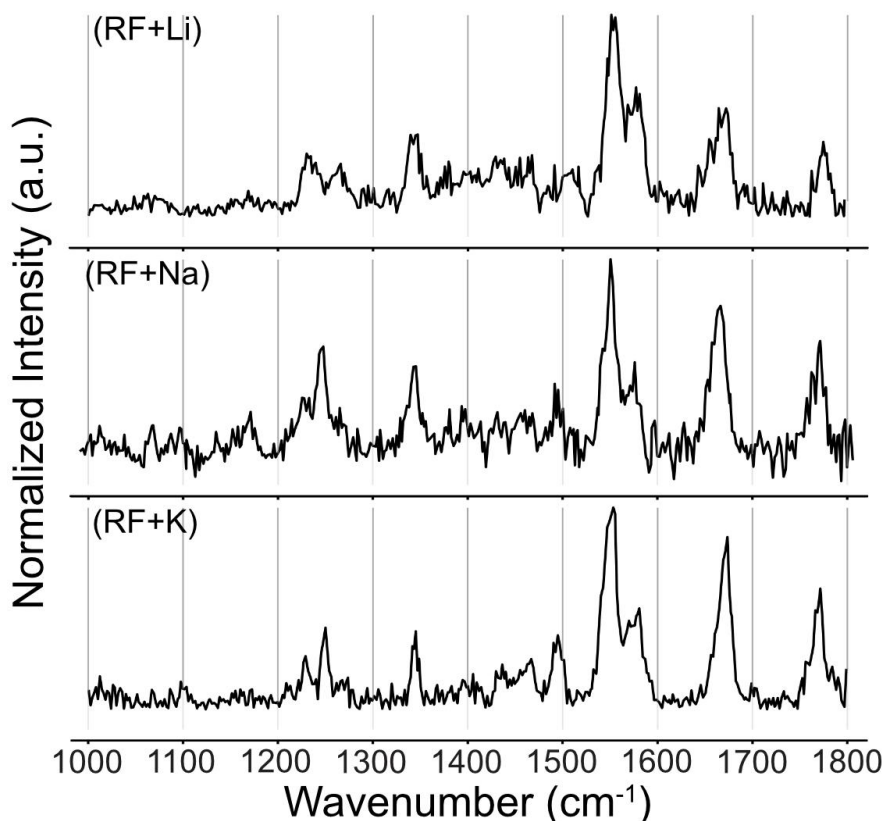


Figure 20: Experimental IR spectra of all measured metal ion riboflavin complexes.

Indeed the opposite resulted out of the taken measurements. As graphic 20 evaluates, the measured IR spectra of the metal ion riboflavin complexes look nearly alike, looking at peak position and intensity. The calculations show that the best fitting theoretical structures of all metal ion riboflavin complexes hold the added atom at the same position. Even though the attachment of the alkali atom near the C=O-Bond at position (19) was expected, it was surprising to see no significant change in wavenumber for the peak that holds the C=O stretching vibration at position (19) of the molecule. Due to the resolution of the experiment it is not possible to see if the peak appears in a significant and logical order for the different complexes. The peak appears around  $1668\text{ cm}^{-1}$  for riboflavin lithium complexes,  $1665\text{ cm}^{-1}$  for riboflavin sodium complexes and  $1674\text{ cm}^{-1}$  for riboflavin potassium complexes. These differences are even too small to say that the peak position differs at all. Looking at their ion mobility it is indeed possible to see some differences. From lightest to heaviest attached alkali atom they appear in figure 21, which shows the intensity over their drift time. The riboflavin lithium complex appears first, as lithium is the lightest atom, up to riboflavin potassium complexes, which is the heaviest out of the measured ones. Even though riboflavin lithium and sodium complexes do not differ that much and do mostly overlap. Which might be a mixture of measurement inaccuracy or resolution, or the fact that lithium and sodium do not differ much in their mass compared to the difference they have towards potassium. The measured CCS values of the complexes show the same relation. The riboflavin lithium complex has

the lowest CCS value of 117.9 Å, the riboflavin sodium complex has a CCS value of 119,2 Å and the riboflavin potassium complex has a value of 121,5 Å.

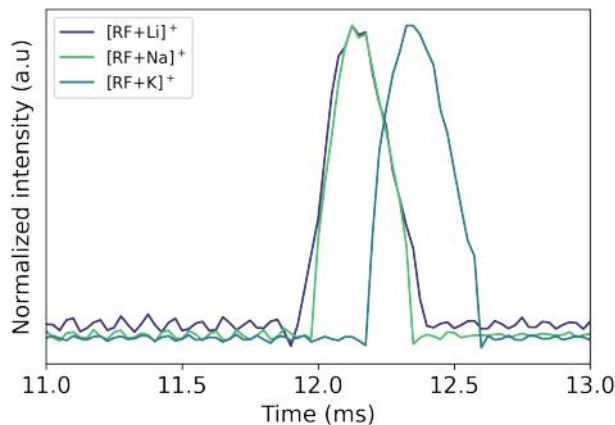


Figure 21: Arrival Time Distribution of all metal ion riboflavin complexes.

## 5 Conclusion

Within this bachelor thesis riboflavin complexes were measured with messenger tagging action spectroscopy and ion mobility spectrometry. In total four cold ion IR spectra were measured i.e., of protonated riboflavin and riboflavin lithium, sodium and potassium complexes, respectively. Furthermore, the protonation sites of protonated riboflavin were observed using ion mobility on two different experimental setups. First it was observed at the iMob instrument. Looking at the ion mobility for protonated riboflavin on the iMob instrument showed different arrival times. Just one arrival time peak showed the mass over charge value 377 m/z of protonated riboflavin. Checking the sample at the TIMS instrument (higher resolution), also showed only one peak in the mobilogram of riboflavin. Thus, contrary to what was expected and predicted to be very likely by literature, no conformation towards the existence of more than one protonation site of riboflavin was found. This can be explained through the structural conformation of the protonation sites differing very little and thus showing similar CCS values. Alternatively, only one protonation site of protonated riboflavin exists and is thermodynamically favored. It was possible to measure a well resolved spectrum of protonated riboflavin to which a matching theoretical spectrum was calculated, at the wB97XD/def2-TZVP level of theory. The calculations evidently show that the protonated riboflavin spectra corresponds to structure 1<sub>RF+H</sub>. While preparing the measurements of the IR spectra and especially while preparing the measurements of the metal ion riboflavin complexes, the tagging conditions and cryogenic ion trap parameters for each measured complex were investigated and determined. The investigation revealed general experimental conditions for biomolecules. For the riboflavin-metal complexes it was expected to observe significant differences in their spectra due to their different masses and interaction strengths. Comparing all three experimental spectra that were taken, revealed no significant differences. Especially a shift in wavenumber was expected for



the peak that holds the C=O-Stretching vibration, to which the alkali atom is attached. It was not possible to observe a significant change in wavenumber for this peak, the changes were around  $6\text{ cm}^{-1}$ . These changes are very small and cannot be confidently interpreted within the resolution of the experiment. To conclude it is not observable that the peak position changes in wavenumber in a significant way or if the wavenumber of this peak changes at all, as the iMob instrument is not able to resolve changes in wavenumber that small. Else, it was possible to see differences between the measured complexes by looking at their ion mobility. The calculated and measured CCS values as well as the arrival time distribution (figure 21) for those complexes showed: the higher the mass of the added atom the higher the CCS value and the higher the arrival time of the complex. This indicates unfolding and weaker interactions from lithium to potassium.

## 6 Acknowledgement

Ich möchte mich bei allen bedanken, die mich beim Schreiben dieser Arbeit unterstützt haben. Bedanken möchte ich mich bei Prof. Dr. Gert von Helden, für die Möglichkeit die Bachelorarbeit seiner Arbeitsgruppe zu schreiben und die gute Betreuung. Bei Prof. Dr. Kevin Pagel und Prof. Dr. Gert von Helden möchte ich mich außerdem für die angenehme und konstruktive Atmosphäre innerhalb der Gruppe bedanken.

Mein Dank gilt auch Prof. Dr. Gerard Meijer für das fungieren als Erstkorrektor für diese Arbeit, die Aufnahme in die Abteilung Molekülphysik des Fritz Haber Instituts und das Bereitstellen der Infrastruktur. Für das fungieren als Zweitkorrektor möchte ich außerdem Prof. Dr. Tobias Kampfrath danken.

Danke an Dr. Wieland Schöllkopf und Sandy Gewinner für das Betreiben des FHI FEL während der Strahlzeiten.

Ein besonderer Dank geht an Jerome Riedel für die ganze Unterstützung während meiner Zeit am FHI, bei den Experimenten und den Berechnungen für die Arbeit, für das Motivieren und die Gespräche über die Arbeit und Persönliches.

Bei Jan Horlebein bedanke ich mich für die tatkräftige Unterstützung beim tunen und den Strahlzeiten und die vielen freundschaftlichen Gespräche.

Ich möchte mich bei Katja Ober, América Torres-Boys, Dr. Martín Taccone, Dr. Gergő Péter Szekeres, Maike Lettow, Carla Kirschbaum und Kim Greis für das freundschaftliche Miteinander und auch dem Rest der Helden-Pagel-Gruppe danke ich für die anregende Arbeitsatmosphäre und den produktiven Austausch.

Außerdem möchte ich mich bei meinen Freunden bedanken, besonders bei Alexa, Noemi, Tona und Wanda, dafür dass ihr immer ein offenes Ohr für mich habt.

Meinen Eltern danke ich für die ganze Unterstützung während des Studiums, danke für die vielen Gespräche über Mathematik und Physik, für die vielen motivierende Worte und danke, dass ihr an mich glaubt. Danke auch an meine Geschwister: Ben, Felix und Ida.

Danke Marian, dass du für mich da bist. Danke für das Motivieren und Aufmuntern. Danke, dass du mir immer zuhörst, auch wenn ich mich mal wieder verzweifelt über mein vermeintlich schlechtes Zeitmanagement beschwere.

## References

- [1] Jeng-Da Chai and Martin Head-Gordon. “Long-range corrected hybrid density functionals with damped atom–atom dispersion corrections”. In: *Phys. Chem. Chem. Phys.* 10 (44 2008), pp. 6615–6620. DOI: 10.1039/B810189B. URL: <http://dx.doi.org/10.1039/B810189B>.
- [2] Jeng-Da Chai and Martin Head-Gordon. “Systematic optimization of long-range corrected hybrid density functionals”. In: *The Journal of chemical physics* 128.8 (2008), p. 084106.
- [3] Ziran Chen et al. “Theoretical investigations on charge transport properties of tetrabenzo [a,d,j,m] coronene derivatives using different density functional theory functionals (B3LYP, M06-2X, and wB97XD)”. In: *Journal of Chemical Research* 43.7-8 (2019), pp. 293–303. DOI: 10.1177/1747519819861626. eprint: <https://doi.org/10.1177/1747519819861626>. URL: <https://doi.org/10.1177/1747519819861626>.
- [4] Reiner M. Dreizler and Cora S. Lüdde. “A Safari Through Density Functional Theory”. In: *Exciting Interdisciplinary Physics: Quarks and Gluons / Atomic Nuclei / Relativity and Cosmology / Biological Systems*. Ed. by Walter Greiner. Heidelberg: Springer International Publishing, 2013, pp. 465–478. ISBN: 978-3-319-00047-3. DOI: 10.1007/978-3-319-00047-3\_37. URL: [https://doi.org/10.1007/978-3-319-00047-3\\_37](https://doi.org/10.1007/978-3-319-00047-3_37).
- [5] Martin Badertscher Ernö Pretsch Philippe Bühlmann. *Spektroskopische Daten zur Strukturaufklärung organischer Verbindungen*. Springer Spektrum Berlin, Heidelberg, 2020.
- [6] Hossein Farrokhpour and Hamidreza Jouypazadeh. “Description of adenine and cytosine on Au(111) nano surface using different DFT functionals (PW91PW91, wB97XD, M06-2X, M06-L and CAM-B3LYP) in the framework of ONIOM scheme: Non-periodic calculations”. In: *Chemical Physics* 488-489 (2017), pp. 1–10. ISSN: 0301-0104. DOI: <https://doi.org/10.1016/j.chemphys.2017.03.001>. URL: <https://www.sciencedirect.com/science/article/pii/S0301010416306851>.
- [7] V. Fock. “Näherungsmethode zur Lösung des quantenmechanischen Mehrkörperproblems”. In: *Zeitschrift für Physik* 61.5 (1930), pp. 126–148.
- [8] MJ ea Frisch et al. *Gaussian 16*. 2016.
- [9] SC Gottschalk et al. “Design and Performance of the Wedged Pole Hybrid Undulator for the Fritz-Haber-Institut IR FEL”. In: *34th International Free Electron Laser Conference*. 2013, pp. 575–578.
- [10] D. R. Hartree. “The Wave Mechanics of an Atom with a Non-Coulomb Central Field. Part I. Theory and Methods”. In: *Mathematical Proceedings of the Cambridge Philosophical Society* 24.1 (1928), 89–110. DOI: 10.1017/S0305004100011919.
- [11] William M Haynes, David R Lide, and Thomas J Bruno. *CRC handbook of chemistry and physics*. CRC press, 2016.

- [12] Vanessa Hinnenkamp et al. "Comparison of CCS Values Determined by Traveling Wave Ion Mobility Mass Spectrometry and Drift Tube Ion Mobility Mass Spectrometry". In: *Analytical Chemistry* 90.20 (2018). PMID: 30215509, pp. 12042–12050. DOI: 10.1021/acs.analchem.8b02711. eprint: <https://doi.org/10.1021/acs.analchem.8b02711>. URL: <https://doi.org/10.1021/acs.analchem.8b02711>.
- [13] P. Hohenberg and W. Kohn. "Inhomogeneous Electron Gas". In: *Phys. Rev.* 136 (3B 1964), B864–B871. DOI: 10.1103/PhysRev.136.B864. URL: <https://link.aps.org/doi/10.1103/PhysRev.136.B864>.
- [14] J. Horlebein. "Characterisation of Cold and Isolated Biomolecules". In: (2022). Master Thesis, Fritz-Haber Institute, Berlin.
- [15] Christian Ieritano et al. "A parallelized molecular collision cross section package with optimized accuracy and efficiency". In: *Analyst* 144.5 (2019), pp. 1660–1670.
- [16] Christian Ieritano et al. "A parallelized molecular collision cross section package with optimized accuracy and efficiency". In: *Analyst* 144.5 (2019), pp. 1660–1670.
- [17] Herbert F. Shurvell David A. Lightner Joseph B. Lambert Scott Gronert. *Spektroskopie - Strukturaufklärung in der Organischen Chemie*. Pearson Studium, 2012.
- [18] Judith Langer et al. "Probing Protonation Sites of Isolated Flavins Using IR Spectroscopy: From Lumichrome to the Cofactor Flavin Mononucleotide". In: *ChemPhysChem* 15.12 (2014), pp. 2550–2562. DOI: <https://doi.org/10.1002/cphc.201402146>. eprint: <https://chemistry-europe.onlinelibrary.wiley.com/doi/pdf/10.1002/cphc.201402146>. URL: <https://chemistry-europe.onlinelibrary.wiley.com/doi/abs/10.1002/cphc.201402146>.
- [19] Francesco Lanucara et al. "The power of ion mobility-mass spectrometry for structural characterization and the study of conformational dynamics". In: *Nature chemistry* 6.4 (2014), pp. 281–294.
- [20] M. Lettow. "Fucosylated and Sulfated Glycans Investigated using Cryogenic Infrared Spectroscopy". In: (2022). Ph.D. Thesis, Radboud University, Nijmegen, the Netherlands.
- [21] Christopher B. Martin et al. "The Reaction of Triplet Flavin with Indole. A Study of the Cascade of Reactive Intermediates Using Density Functional Theory and Time Resolved Infrared Spectroscopy". In: *Journal of the American Chemical Society* 124.24 (2002). PMID: 12059249, pp. 7226–7234. DOI: 10.1021/ja0123711. eprint: <https://doi.org/10.1021/ja0123711>. URL: <https://doi.org/10.1021/ja0123711>.
- [22] MF Mesleh et al. "Structural information from ion mobility measurements: effects of the long-range potential". In: *The Journal of Physical Chemistry* 100.40 (1996), pp. 16082–16086.

- [23] Karsten Michelmann et al. “Fundamentals of Trapped Ion Mobility Spectrometry”. In: *Journal of the American Society for Mass Spectrometry* 26.1 (2015). PMID: 25331153, pp. 14–24. DOI: 10.1007/s13361-014-0999-4. eprint: <https://doi.org/10.1007/s13361-014-0999-4>. URL: <https://doi.org/10.1007/s13361-014-0999-4>.
- [24] Chr. Møller and M. S. Plesset. “Note on an Approximation Treatment for Many-Electron Systems”. In: *Phys. Rev.* 46 (7 1934), pp. 618–622. DOI: 10.1103/PhysRev.46.618. URL: <https://link.aps.org/doi/10.1103/PhysRev.46.618>.
- [25] PM Morse. “Diatomic molecules according to the wave mechanics. II. Vibrational levels. PHYSICAL REVIEW, v. 34, pp. 57-64”. In: (1929).
- [26] Eike Mucha et al. “Glycan Fingerprinting via Cold-Ion Infrared Spectroscopy”. In: *Angewandte Chemie International Edition* 56.37 (2017), pp. 11248–11251. DOI: <https://doi.org/10.1002/anie.201702896>. eprint: <https://onlinelibrary.wiley.com/doi/pdf/10.1002/anie.201702896>. URL: <https://onlinelibrary.wiley.com/doi/abs/10.1002/anie.201702896>.
- [27] K. Ober. “Spectroscopy of deprotonation dynamics in helium droplets”. In: (2021). Master Thesis, Freie Universität Berlin, Fritz-Haber Institute, Berlin.
- [28] John T Pinto and Janos Zemleni. “Riboflavin”. In: *Advances in Nutrition* 7.5 (Sept. 2016), pp. 973–975. ISSN: 2161-8313. DOI: 10.3945/an.116.012716. eprint: <https://academic.oup.com/advances/article-pdf/7/5/973/23754828/an012716.pdf>. URL: <https://doi.org/10.3945/an.116.012716>.
- [29] Philipp Pracht, Fabian Bohle, and Stefan Grimme. “Automated exploration of the low-energy chemical space with fast quantum chemical methods”. In: *Physical Chemistry Chemical Physics* 22.14 (2020), pp. 7169–7192.
- [30] Philipp Pracht and Stefan Grimme. “Calculation of absolute molecular entropies and heat capacities made simple”. In: *Chemical science* 12.19 (2021), pp. 6551–6568.
- [31] *Precomputed vibrational scaling factors*. <https://cccbdb.nist.gov/vibscalejust.asp>. Accessed: 2022-10-03.
- [32] George D. Purvis and Rodney J. Bartlett. “A full coupled-cluster singles and doubles model: The inclusion of disconnected triples”. In: *The Journal of Chemical Physics* 76.4 (1982), pp. 1910–1918. DOI: 10.1063/1.443164. eprint: <https://doi.org/10.1063/1.443164>. URL: <https://doi.org/10.1063/1.443164>.
- [33] Daniel Püschner. *Quantitative Rechenverfahren Der Theoretischen Chemie*. Springer, 2017.
- [34] W Schöllkopf et al. “Advances in X-Ray Free-Electron Lasers Instrumentation III, Vol. 9512”. In: Spie-Int. Soc Optical Engineering Bellingham. 2015.
- [35] Wieland Schöllkopf et al. “The FHI FEL upgrade design”. In: *39th International Free-Electron Laser Conference (FEL2019)*. JACoW. 2019, pp. 52–55.

- [36] Wieland Schöllkopf et al. “The new IR and THz FEL facility at the Fritz Haber Institute in Berlin”. In: *Advances in X-ray Free-Electron Lasers Instrumentation III*. Vol. 9512. SPIE. 2015, pp. 238–250.
- [37] Erwin Schrödinger. “Quantisierung als eigenwertproblem”. In: *Annalen der physik* 385.13 (1926), pp. 437–490.
- [38] Sevugarajan Sundarapandian, Jody C. May, and John A. McLean. “Dual Source Ion Mobility-Mass Spectrometer for Direct Comparison of Electrospray Ionization and MALDI Collision Cross Section Measurements”. In: *Analytical Chemistry* 82.8 (2010). PMID: 20329759, pp. 3247–3254. DOI: 10.1021/ac902980r. eprint: <https://doi.org/10.1021/ac902980r>. URL: <https://doi.org/10.1021/ac902980r>.
- [39] Daniel A. Thomas et al. “Characterization of a trans–trans Carbonic Acid–Fluoride Complex by Infrared Action Spectroscopy in Helium Nanodroplets”. In: *Journal of the American Chemical Society* 141.14 (2019). PMID: 30883095, pp. 5815–5823. DOI: 10.1021/jacs.8b13542. eprint: <https://doi.org/10.1021/jacs.8b13542>. URL: <https://doi.org/10.1021/jacs.8b13542>.
- [40] Kamil Uludag et al. “Crosstalk in the Lambert-Beer calculation for near-infrared wavelengths estimated by Monte simulations”. In: *Journal of Biomedical Optics* 7.1 (2002), pp. 51–59. DOI: 10.1117/1.1427048. URL: <https://doi.org/10.1117/1.1427048>.
- [41] Leandro Zanutto et al. *High performance collision cross section calculation—HPCCS*. 2018.

## A *CREST* input parameters

Table 1: Specification of *CREST* command line invocations used in protonation and alkalation site screening.

Adduct	Command line invocation
RF-H	<code>crest riboflavin.xyz --protonate</code>
RF-Li	<code>crest riboflavin.xyz --protonate --swel li+</code>
RF-Na	<code>crest riboflavin.xyz --protonate --swel na+</code>
RF-K	<code>crest riboflavin.xyz --protonated --swel k+</code>

Table 2: Specification of *CREST* command line parameters used in the conformational search for the different protonated and alkalated input structures.

Parameter	Value	Description
v4		Demands the iMTD-SMTD workflow in the conformational search
chrg	1	Charge of the input structure
len	1.5	Increased length of the meta-dynamics search by 50% compared to the automatically determined value

## B Experimental and theoretical CCS values

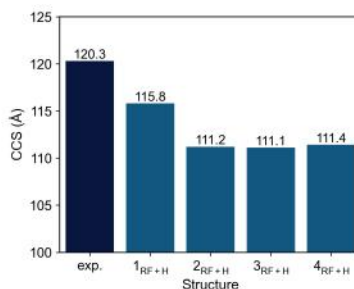


Figure 22: CCS values of protonated riboflavin theory and experiment.

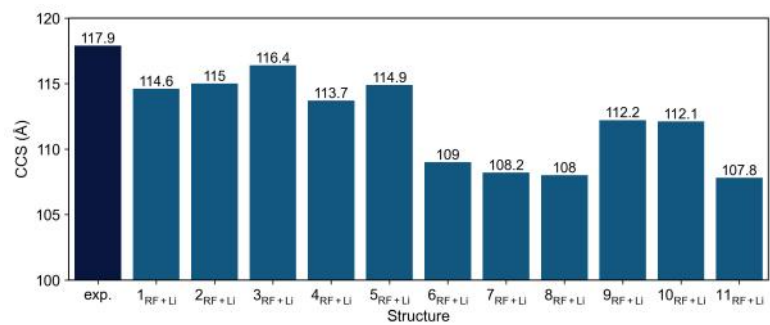


Figure 23: CCS values of riboflavin lithium complexes theory and experiment.

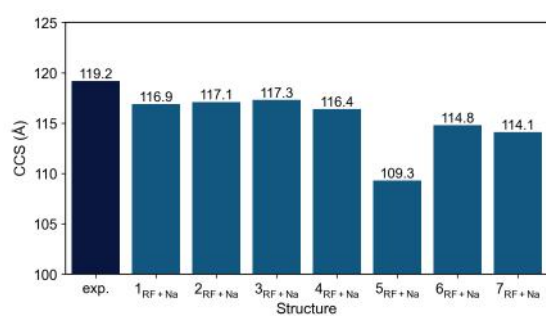


Figure 24: CCS values of riboflavin sodium complexes theory and experiment.

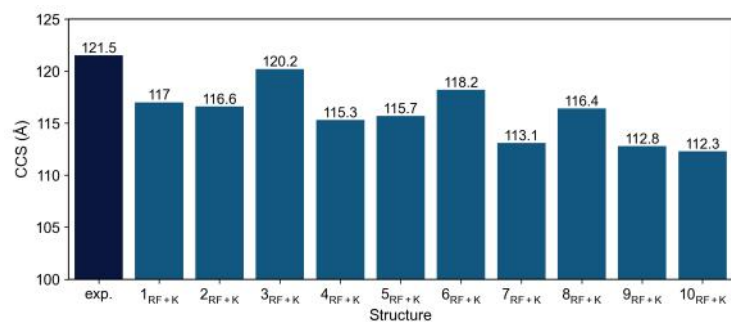


Figure 25: CCS values of riboflavin potassium complexes theory and experiment.



## C Theoretical IR spectra

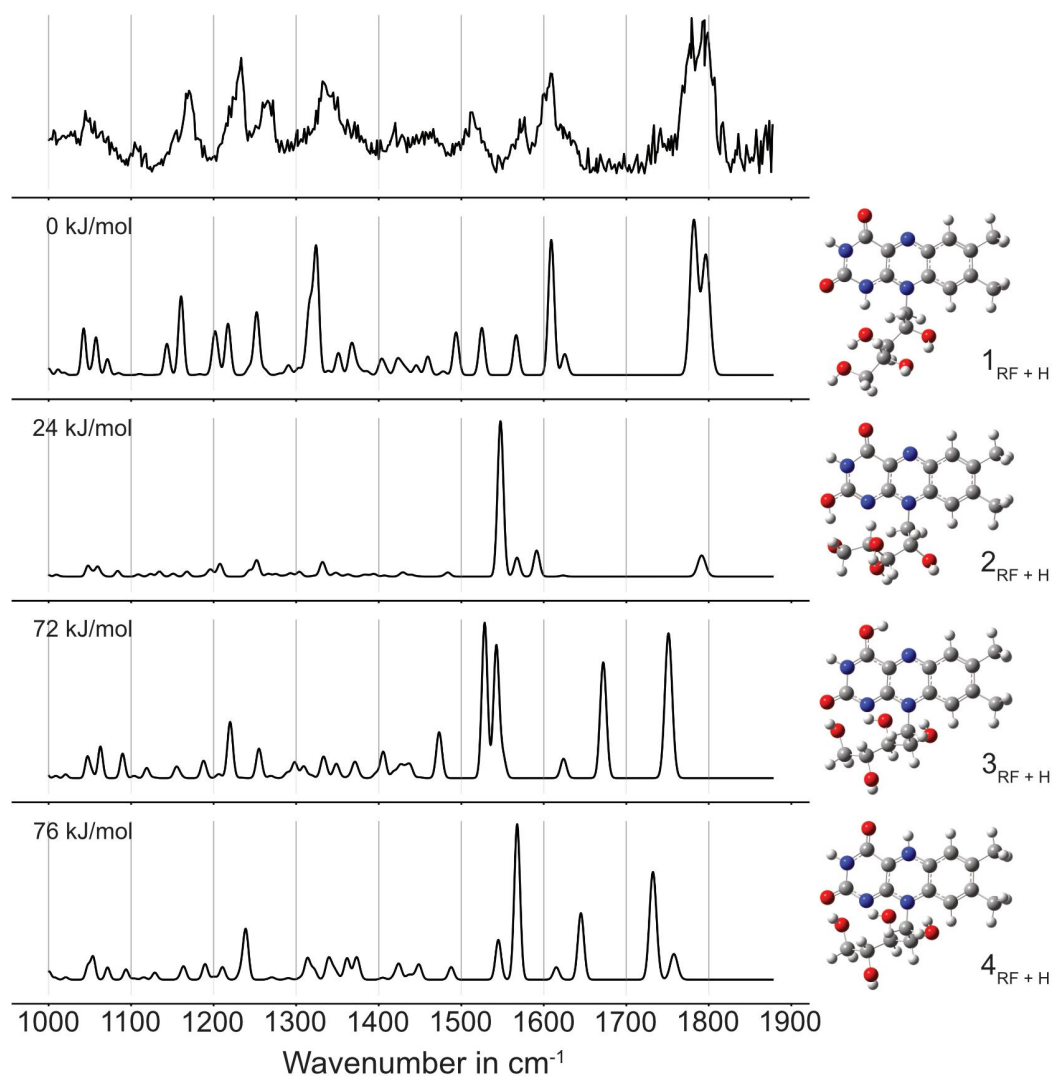


Figure 26: Theoretical IR spectra of protonated riboflavin at the wB97XD/def2-TZVP level of theory.

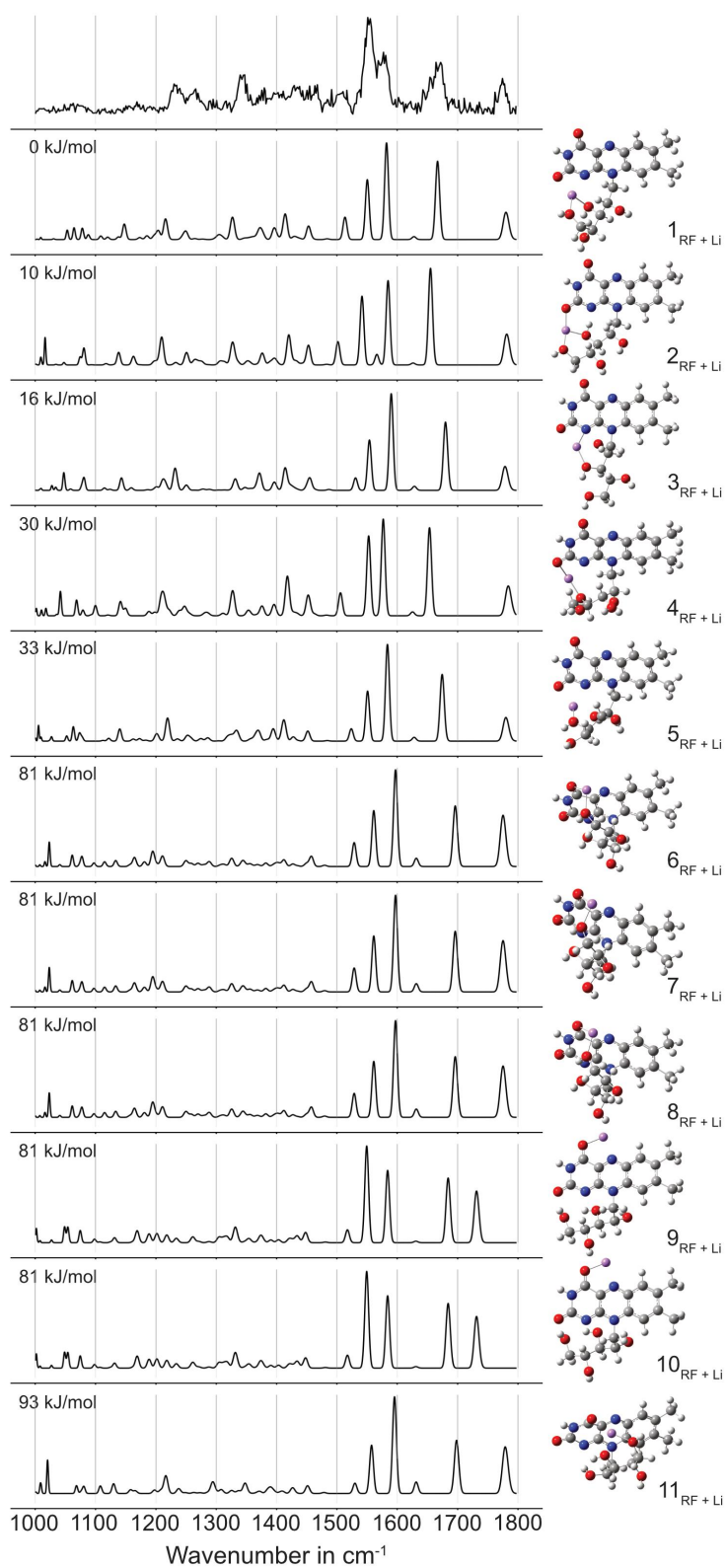


Figure 27: Theoretical IR spectra of riboflavin lithium complexes at the wB97XD/def2-TZVP level of theory.

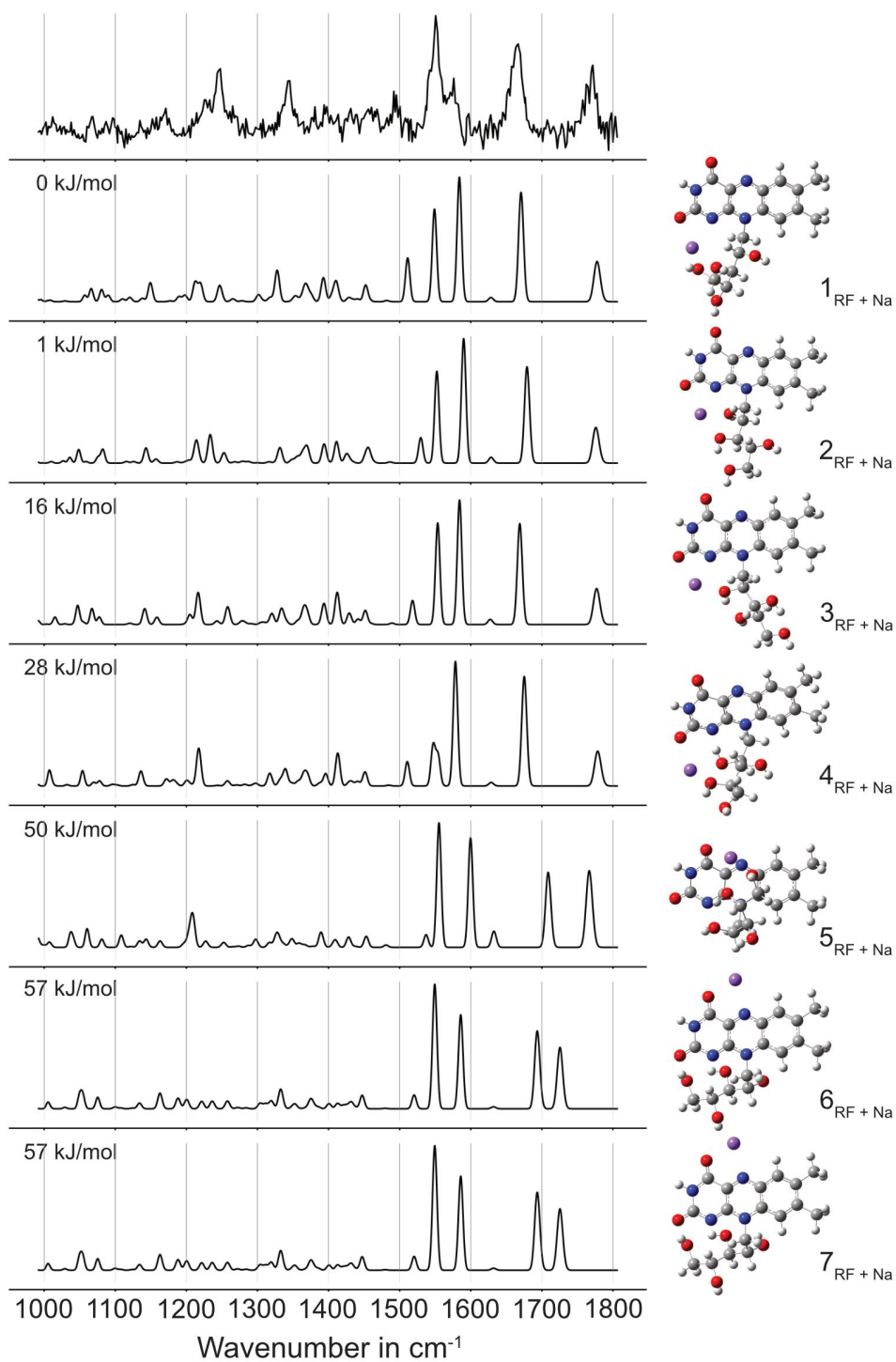


Figure 28: Theoretical IR spectra of riboflavin sodium complexes at the wB97XD/def2-TZVP level of theory.

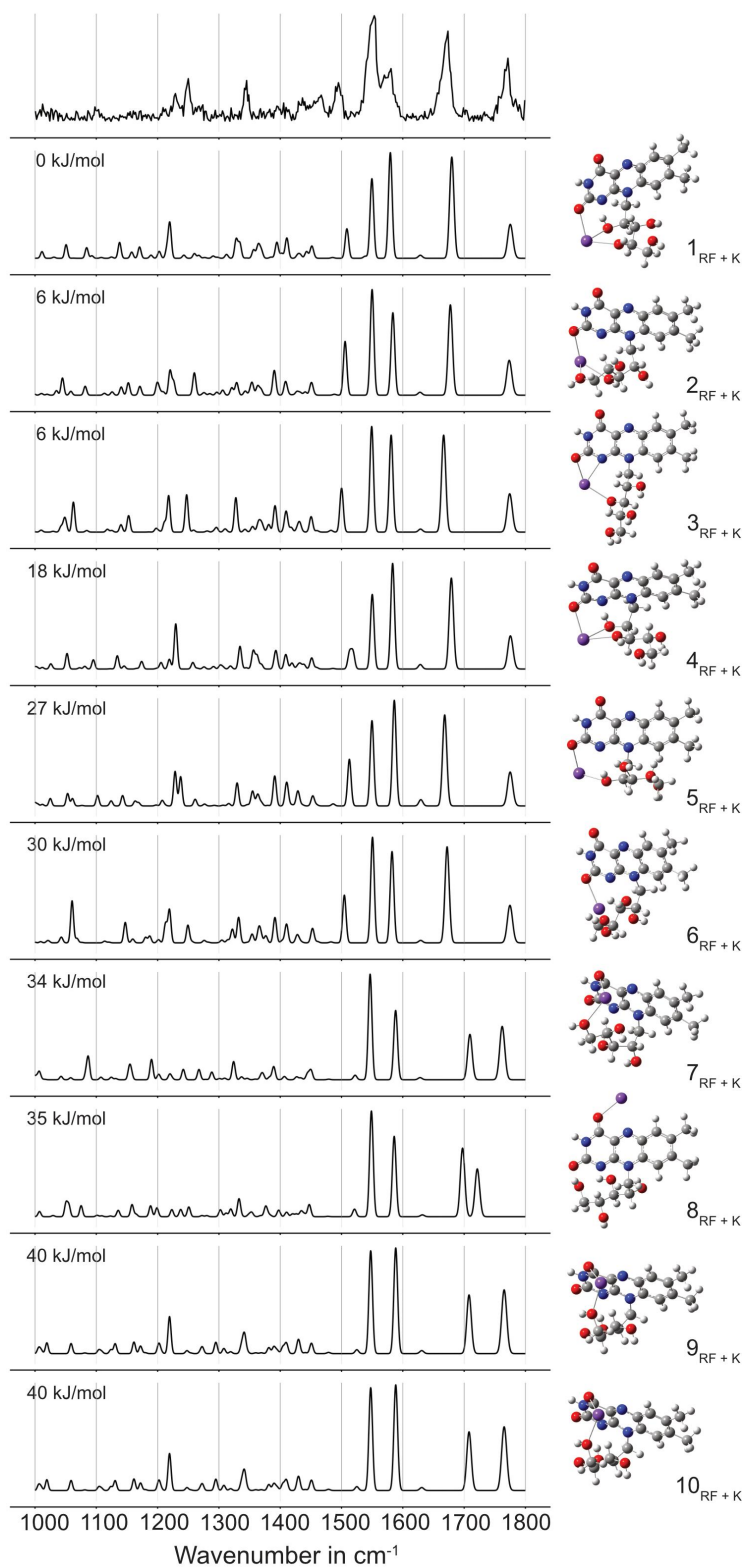


Figure 29: Theoretical IR spectra of riboflavin potassium complexes at the wB97XD/def2-TZVP level of theory.

## D Theoretical calculated structures

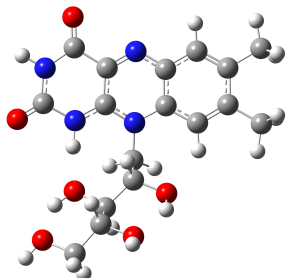


Figure 30: Structure  $1_{RF+H}$  of protonated riboflavin.

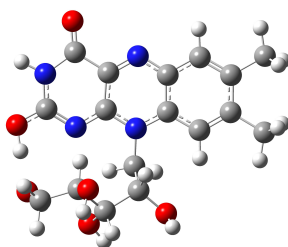


Figure 31: Structure  $2_{RF+H}$  of protonated riboflavin.

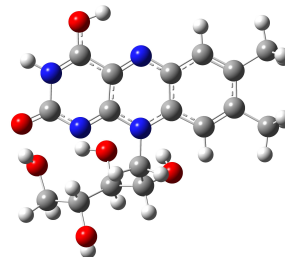


Figure 32: Structure  $3_{RF+H}$  of protonated riboflavin.

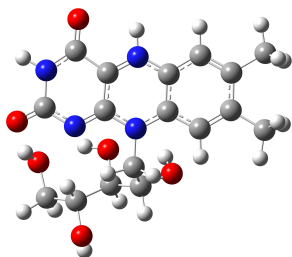


Figure 33: Structure  $4_{RF+H}$  of protonated riboflavin.

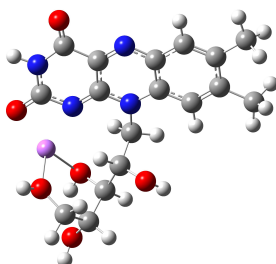


Figure 34: Structure  $1_{RF+Li}$  of the riboflavin lithium complex.

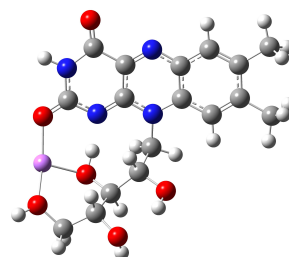


Figure 35: Structure  $2_{RF+Li}$  of the riboflavin lithium complex.

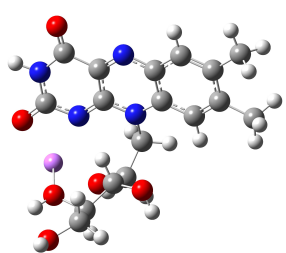


Figure 36: Structure  $3_{RF+Li}$  of the riboflavin lithium complex.

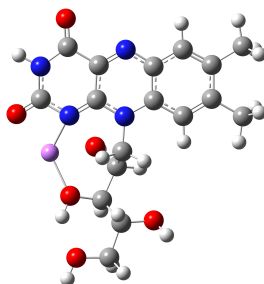


Figure 37: Structure  $4_{RF+Li}$  of the riboflavin lithium complex.

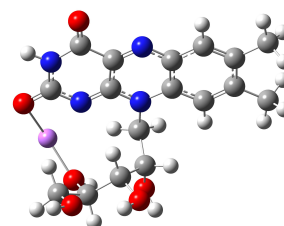


Figure 38: Structure  $5_{RF+Li}$  of the riboflavin lithium complex.

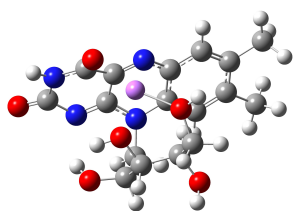


Figure 39: Structure  $6_{RF+Li}$  of the riboflavin lithium complex.

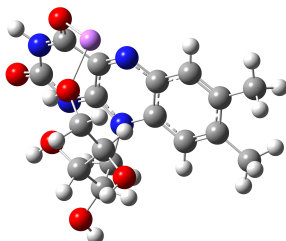


Figure 40: Structure  $7_{RF+Li}$  of the riboflavin lithium complex.

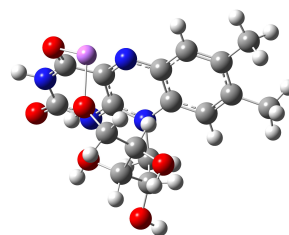


Figure 41: Structure  $8_{RF+Li}$  of the riboflavin lithium complex.

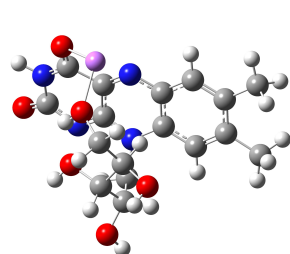


Figure 42: Structure  $9_{RF+Li}$  of the riboflavin lithium complex.

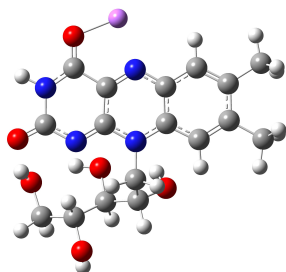


Figure 43: Structure  $10_{RF+Li}$  of the riboflavin lithium complex.

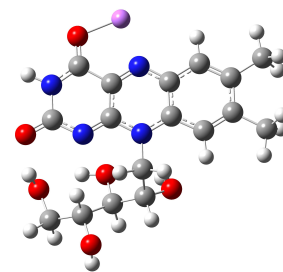


Figure 44: Structure  $11_{RF+Li}$  of the riboflavin lithium complex.

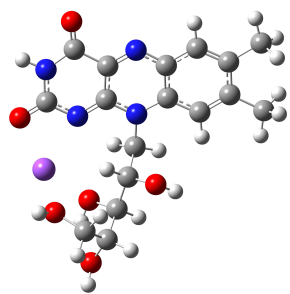


Figure 45: Structure  $1_{RF+Na}$  of the riboflavin sodium complex.

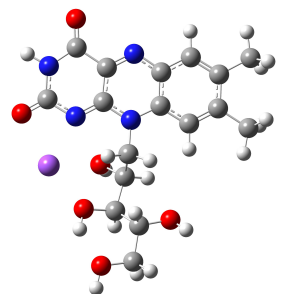


Figure 46: Structure  $2_{RF+Na}$  of the riboflavin sodium complex.

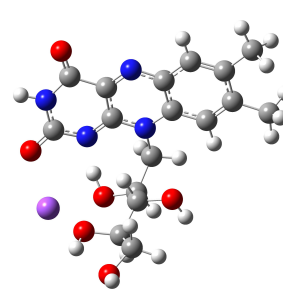


Figure 47: Structure  $3_{RF+Na}$  of the riboflavin sodium complex.

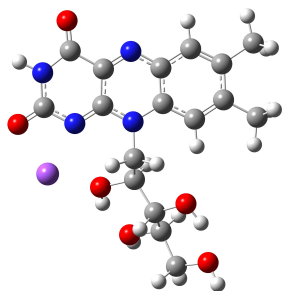


Figure 48: Structure  $4_{RF+Na}$  of the riboflavin sodium complex.

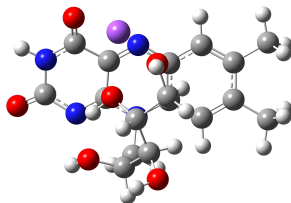


Figure 49: Structure  $5_{RF+Na}$  of the riboflavin sodium complex.

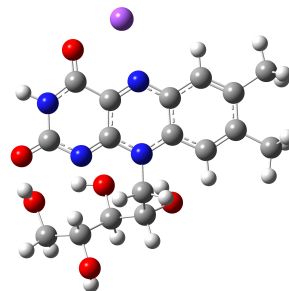


Figure 50: Structure  $6_{RF+Na}$  of the riboflavin sodium complex.

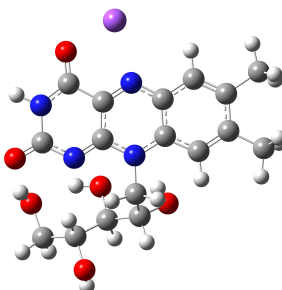


Figure 51: Structure  $7_{RF+Na}$  of the riboflavin sodium complex.

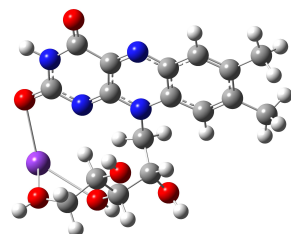


Figure 52: Structure  $1_{RF+K}$  of the riboflavin potassium complex.

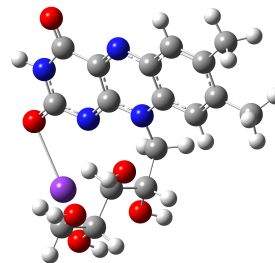


Figure 53: Structure  $2_{RF+K}$  of the riboflavin potassium complex.

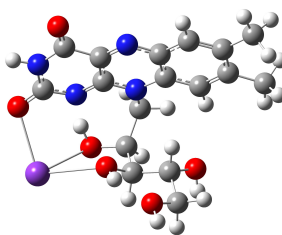


Figure 54: Structure  $3_{RF+K}$  of the riboflavin potassium complex.

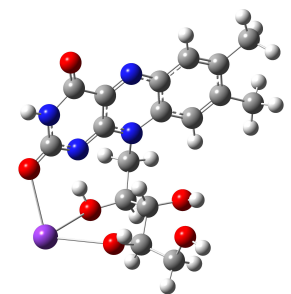


Figure 55: Structure  $4_{RF+K}$  of the riboflavin potassium complex.

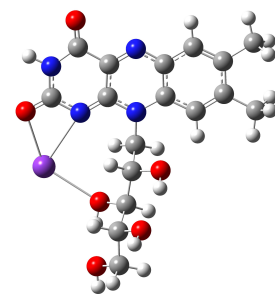


Figure 56: Structure  $5_{RF+K}$  of the riboflavin potassium complex.

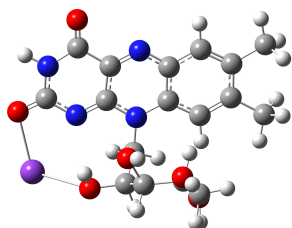


Figure 57: Structure  $6_{RF+K}$  of the riboflavin potassium complex.

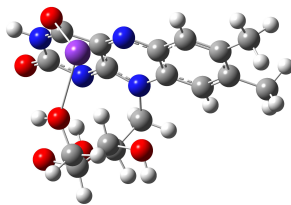


Figure 58: Structure  $7_{RF+K}$  of the riboflavin potassium complex.

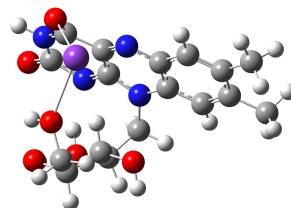


Figure 59: Structure  $8_{RF+K}$  of the riboflavin potassium complex.

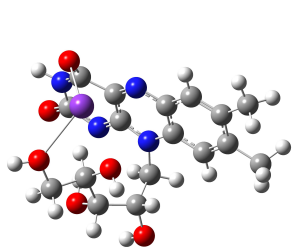


Figure 60: Structure  $9_{RF+K}$  of the riboflavin potassium complex.

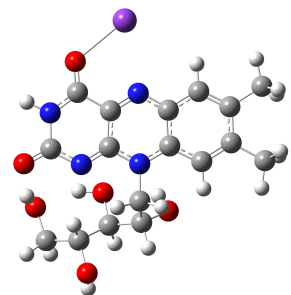


Figure 61: Structure  $10_{RF+K}$  of the riboflavin potassium complex.



## **Selbständigkeitserklärung zur Bachelorarbeit**

Ich erkläre ausdrücklich, dass es sich bei der von mir eingereichten schriftlichen Arbeit, mit dem Titel Messenger Tagging IR Spectroscopy of Gas-Phase Riboflavin Complexes, um eine von mir selbst und ohne unerlaubte Beihilfe verfasste Originalarbeit handelt.

Ich bestätige überdies, dass die Arbeit als Ganze oder in Teilen nicht zur Abgeltung anderer Studienleistungen eingereicht worden ist.

Ich erkläre ausdrücklich, dass ich sämtliche in der oben genannten Arbeit enthaltenen Bezüge auf fremde Quellen (einschließlich Tabellen, Grafiken u. Ä.) als solche kenntlich gemacht habe. Insbesondere bestätige ich, dass ich nach bestem Wissen sowohl bei wörtlich übernommenen Aussagen (Zitaten) als auch bei in eigenen Worten wiedergegebenen Aussagen anderer Autorinnen oder Autoren (Paraphrasen) die Urheberschaft angegeben habe.

Ich nehme zur Kenntnis, dass Arbeiten, welche die Grundsätze der Selbständigkeitserklärung verletzen – insbesondere solche, die Zitate oder Paraphrasen ohne Herkunftsangaben enthalten –, als Plagiat betrachtet werden können.

Ich bestätige mit meiner Unterschrift die Richtigkeit dieser Angaben.

